Master's Thesis

Characterization of Mechanical Micro-Damage in Composite Materials using Acoustic Emission Monitoring and Micro-CT

Leonard Hohaus

TU Delft

Thesis for the degree of MSc in Marine Technology in the specialization of Ship and Offshore Structures

Characterization of Mechanical Micro-Damage in Composite Materials using Acoustic Emission Monitoring and Micro-CT

by

Leonard Hohaus

to obtain the degree of Master of Science
at the Delft University of Technology
to be defended publicly on June 20, 2025.

This thesis (**MT.24/25/042.M**) is classified as confidential in accordance with the general conditions for projects performed by the TUDelft.

Thesis exam committee:	
Chair:	Dr. L. Pahlavan
Committee Members:	Dr. L. Pahlavan
	Prof. Dr. C. Kassapoglou
	Dr. A. Huijer
	Dr. Y. Mosleh
Place:	Faculty of Mechanical Engineering, Delft
Project Duration:	November, 2024 - June, 2025
Author details:	
Student number:	6084559

Abstract

The use of fiber-reinforced composite materials in marine applications is limited by uncertainty surrounding their long-term fatigue behavior and micro-damage tolerance. This thesis aims to present and validate an experimental framework to detect and classify mechanical micro-damage in unidirectional carbon-fiber composites using acoustic emission (AE) monitoring and X-ray micro-computed tomography (micro-CT). AE monitoring provides real-time insight into the evolution of internal damage by capturing elastic waves emitted during micro-structural failure events, while micro-CT offers high-resolution visualization of internal damage states before and after mechanical loading. A comprehensive analysis was conducted involving signal processing, (normalized) frequency spectrum characterization, and unsupervised machine learning to classify AE events by damage type. This classification was subsequently validated against micro-CT scans. Results challenge the common assumption that AE signals with dominant low-frequency contributions are reliably indicative of matrix cracking. The proposed AE framework, when validated with micro-CT, shows promise for enabling accurate in-situ damage monitoring of composite structures in offshore environments. This approach supports the broader adoption of composites by improving confidence and knowledge about their structural integrity over time.

Acknowledgements

Thank you to my supervisors, Drs. Pahlavan and Huijer for their weekly practical support and for giving me the space to tackle problems from my own perspective. To Prof. Kassapoglou for his technical expertise, valuable insight, and challenging gaze, always pushing me to further depth. To Hellen Meijvogel for her friendly temperament and her great work on the micro-CT scans.
Thank you to my parents for their unwavering support and for being a daily example of hard work, and to my sister, with her discipline and determination, for always holding me to a higher standard.
Thank you to my sharp, witty, and endlessly clever girlfriend, for not putting up with anyone's nonsense - except for mine. I'm the lucky exception.
Big thanks to my Delft fam, who have given so much color, sound, and substance to my life over the past year. This has been very special to me.

To everyone I shared (parts of) these past two years with, I am tremendously grateful, and I have had so many good times with you. I will forever look back on this period with a big smile on my face.

Contents

Nomenclature

List of Abbreviations

AE	Acoustic Emission
ASL	Average Signal Level
CWT	Continuous Wavelet Transform
DAQ	Data-Acquisition
DTFT	Discrete-Time Fourier Transform
EMD	Empirical Mode Decomposition
FFT	Fast Fourier Transform
FRC	Fiber-Reinforced Composite
GMM	Gaussian Mixture Models
IRT	Infrared Tomography
ML	Machine Learning
NDT	Non-Destructive Testing
OOA	Out-of-Autoclave
PCA	Principal Component Analysis
PLB	Pencil Lead Break
PRIDB	Primary Database
PZT	Lead Zirconate Titanate
RMS	Root Mean Square
RQ	Research Question
SHM	Structural Health Monitoring
STFT	Short-Time Fourier Transform
SVD	Singular Value Decomposition
TDOA	Time Difference of Arrival
TRADB	Transient Database
WPT	Wavelet Packet Transform
XCT	X-ray Computed Tomography

List of Symbols

σ	Stress
ε	Strain
R	Load ratio
v_g	Group velocity of AE wave packets
v_g	Phase velocity of elastic waves
Δt	Time difference of arrival
$x(t)$	Complete recorded waveform signal
$\Psi(t)$	Primary wave packet waveform signal
$\psi(f,\tau)$	Wavelet function
k	Number of clusters
$E_\Psi(f)$	Frequency spectrum of a primary wave packet
$\hat{E}_\Psi(f)$	Normalized frequency spectrum of a primary wave packet

1 Introduction

1.1. Uncertainty Management in the Offshore Industry

Managing uncertainty is one of the major challenges in the offshore industry. The sector is laid out for the long term but regularly faces unpredictable factors such as changing weather, fluctuating costs, and evolving regulations. These conditions demand that companies remain flexible and proactive.
One way to keep ships and structures safe, efficient, and sustainable under these constantly changing conditions is for engineers to continuously adopt advanced technologies like predictive analytics, real-time monitoring systems, and AI-based decision tools. Spotting disruptions early can help maritime companies safeguard their assets, streamline logistics, and ensure compliance.
Composite materials are a class of materials limited heavily in their application by their unpredictable long-term fatigue behavior [1]. Safety, cost, and ensuring operability are factors that sometimes make the application of composite materials prohibitively risky in the maritime industry. Structural health monitoring using acoustic emissions has the potential to unlock new areas of application for these materials, driving technological advancement and opening up market opportunities.

1.2. Composite Ship Hulls and Propellers

Composite marine propellers and ship hulls have the potential to reduce the environmental signature and carbon emissions of maritime vehicles. However, the reaction of composite hulls under high-amplitude impact loads and the fatigue lifetime of composite propeller blades are challenging topics that have not been sufficiently investigated so far. The challenges lie mainly in the high energy of wave impact loads, the complex geometry and loading of the propeller blades, the large number of loading cycles they experience throughout their lifetime, and the diverse material damage mechanisms involved at the micro-scale. It is necessary to demonstrate that composite materials can be safe and reliable before they can be safely deployed in real offshore applications.
Composite materials pose challenges in long-term applications, where cyclic loads and the occurrence of impacts are to be taken into account, largely due to unresolved questions regarding their damage resistance and damage tolerance properties [2]. Damage resistance refers to the ability of a material to avoid the formation of (internal and micro-) damage under conditions of loading and deformation. Damage tolerance is the ability to maintain functionality (structural integrity in the case of structural materials) after damage has occurred. This thesis aims to develop an acoustic monitoring framework designed for both the detection and the classification of micro-damage to support the assessment of resistance and tolerance of composite materials, both in the laboratory and in offshore applications.

1.3. Layout of the Thesis

This report presents the work conducted as part of the experimental Master's thesis titled "Characterization of Mechanical Damage in Composite Materials Using Acoustic Emissions and Micro-CT". The two methods (AE monitoring and micro-CT) provide complementary insights, where AE monitoring will be used to provide a real-time supervision of damage creation, while micro-CT can offer a discrete-time insight with detailed spatial resolution before and after damage has taken place.

Chapter 2 covers scientific literature in the field of fatigue, mechanical (micro-)damage, and structural health monitoring of fiber-reinforced composite materials. The objective was to identify a knowledge gap

(Section 2.4) and a set of research questions laid out in Chapter 3 that have guided the development of the experimental research framework of this thesis. Chapter 4 covers said research framework, which includes quasi-static tensile testing on unidirectional carbon-fiber composite coupon specimens while monitoring acoustic emissions (AEs), micro-CT scanning before and after tensile testing, and the processing of the recorded AE signals and tomographic images. The results of the experimental campaign are presented in Chapter 5 and discussed further in Chapter 6. The main body of the report is concluded with Chapter 7, where the main findings are collected and a novel interpretation laid out. The final chapter of this thesis (Chapter 8) covers recommendations for further work aimed at improving the current benchmark, as well as an outlook on a potential application of the testing and analysis framework, whose feasibility has been evaluated in the scope of this study.

2

Background

2.1. Fatigue of Fiber-Reinforced Composite (FRC) Materials

Composite materials differ from metals in their fatigue behavior. In metals, fatigue is defined as a (near) surface phenomenon and is usually dominated by a finite number of cracks initiating at critical locations and propagating up to fracture. The overall lifetime of a structure is governed by crack nucleation and short crack growth at locations of macroscopic stress concentrations. These can cause the plasticity threshold to be locally exceeded even when applying a sub-yield nominal cyclic stress. The microscopic structure of metals is composed of crystalline grains of uniform atomic composition, and the strength of atomic bonds at the grain interfaces is reduced, creating critical locations for micro-crack initiation and growth [3].
Long fiber composite materials, on the other hand, exhibit a fatigue behavior with additional complexities. Their internal structure is characterized by an inhomogeneous and anisotropic composition on multiple length scales. On the microscopic scale (typical fiber diameter: $5 - 10\mu m$), they are made up of matrix and fiber materials and their bonding interface. On the mesoscale ($0.1 - 0.5mm$), there are plies of different orientations and the inter-ply interfaces between them. Fatigue damage can initiate and grow within any one of these components or interfaces, leading to a variety of different and relevant mechanical degradation and failure mechanisms [4].

Vassilopoulos [5] provides an extensive review of the history of research on the topic of FRC fatigue. In the 1970s and 80s, the understanding of fatigue in composite materials as a phenomenon of creation and growth of internal damage was established. As damage accumulates, the internal structure of the material 'degrades'. Several measures of degradation, so-called damage state metrics, have been used over the decades of research on the topic:
Highsmith and Reifsnider [6], for example, used *residual stiffness* as a running measure of damage and attempted to associate it with remaining lifetime (see Fig. 2.1).

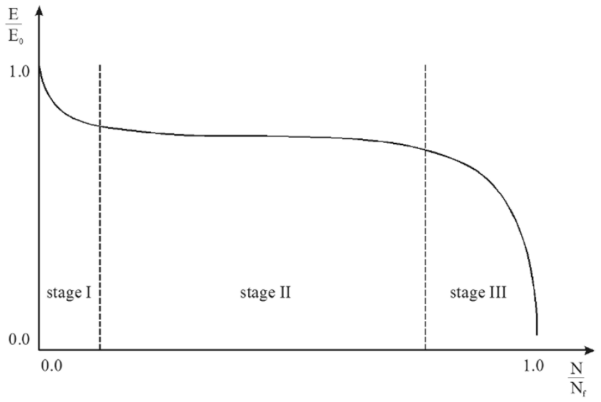

Figure 2.1: Typical stiffness degradation during fatigue life of FRC materials [6].

They identified three stages of fatigue degradation in composite materials dominated by different damage mechanisms. In stage I, matrix cracking is the dominant damage mechanism in cross-ply laminates: cracks

form in the resin matrix, particularly in off-axis plies and create local stress concentrations and redistributions (load is deviated away from the cracked transverse plies). In addition, initial random fiber fractures are expected in the 0°-plies during the first loading cycle, depending on the maximum applied load. These are caused by statistical imperfections present even in the pristine fiber-reinforced material.
Stage II is the stage of progressive damage accumulation, where cracks start to link up and affect the integrity of interfaces. Fiber-matrix debonding and delamination initiate and dominate the degradation of stiffness in this stage.
In the final stage (stage III), fiber breakage becomes the leading damage mode, bringing about a sharp drop in residual stiffness and final structural failure. Final failure shall be expected when the matrix damage reaches a point of saturation, inhibiting successful load transfer and creating cascading fiber failures or shear failure, or when enough fibers reach the end of their cyclic lifetimes.
Highsmith and Reifsnider's narrative of the fatigue life of composite materials is still relevant to today's understanding of tensile fatigue of cross-ply FRCs.

Talreja [7] follows a conventional interpretation of fatigue by applying the well-established fatigue lifetime diagrams (S-N curves) to observed data of fatigue experiments of FRCs. He also uses dominant damage mechanisms to differentiate between types of fatigue progression: He adopts Dharan's [8] division of S-N-diagrams of composites into three regions of interest with markedly different slopes. Fiber breakage dominates failure in the low-cycle (high-strain) fatigue range. Fiber-matrix debonding and radial matrix crack growth are more pronounced in the mid-cycle range, and no initiation/crack arrest in the fatigue limit range. This research is summarized in the graph presented in Fig. 2.2.

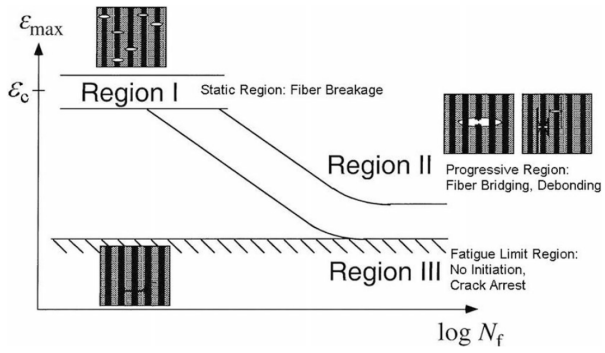

Figure 2.2: Talreja's division of fatigue life diagrams of unidirectional FRCs, and corresponding final-failure-governing damage modes [9].

Talreja & Singh [4] offer a comprehensive guide to the fatigue and failure of composite materials. They elucidate the fundamental principles that govern damage initiation and progression with the help of extensive experimental data. This data shows that fatigue behavior can vary significantly in terms of speed and type of damage progression, even for the same composite material with the same lay-up and the same geometry, depending on internal damage history and random manufacturing defects.

2.1.1. Fatigue Modeling

Different approaches exist for the modeling of fatigue behavior. In his review of existing methods for estimating the fatigue life of fiber-reinforced resin matrix composites, Sendeckyj [10] divides theoretical models into two major categories. The first comprises theories that use statistical descriptions to establish macroscopic failure criteria under constant or variable amplitude fatigue loading (Talreja's approach [7]). This means that mathematical models are used to describe the lifetime data without an apparent physical foundation, but using a rigorous framework that is well-established in the scientific and engineering community. Degrieck and Van Paepagem call this type simply 'fatigue life models' in their review on fatigue life models for composite materials [11].
Sendeckyj's [10] second category includes fatigue theories that take into account the 'physical' development of the internal damage state of the material using a damage metric as an indicator of physical damage accumulation (Reifsnider's approach [6]). Thus, measurements of actual damage metrics can complement

these models during fatigue life testing. A common mechanical damage metric is residual stiffness ([6]). It can be conveniently measured with most fatigue testing setups and reported in a progressive lifetime diagram (see Reifsnider's stiffness-based damage model in Fig. 2.1). Degrieck and Van Paepagem categorize this type of fatigue description as 'phenomenological' fatigue models [11]. Attempts have been made to associate residual stiffness with residual strength, as a secondary, or 'derived' damage state metric ([12]). Residual strength is a useful parameter in practice, but cannot be directly measured without destructive testing of the specimen or part.
Progressive damage models are a third category identified in [11], and they aim to represent the development of the internal damage state and the remaining structural lifetime by modeling intrinsic defects in the matrix and matrix crack growth. Wickanson & Chai [13]'s review covers progressive damage modeling in FRCs, and they also highlight energy release rate as a key metric for predicting damage initiation and propagation.

Vassilopoulos [5] summarizes Sendeckyj's [10] vision of an ideal fatigue theory for FRCs as a damage state model that would be based on a damage metric that accurately represents the observed development of the internal damage state, allow for accurate remaining lifetime estimation based on (two-stage or spectrum) fatigue loading, involves a large class of materials, and accounts for scatter in the data.
Additionally, a desirable feature would be the capability to predict a component's fatigue lifetime using only readily available material properties and design conditions or limited-size quasi-static coupon sample measurement campaigns. A theory that allows to predict the fatigue behavior of large-scale composite structures with confidence without intensive full-scale fatigue testing has not yet, to the knowledge of the author, emerged in the scientific community.

An example of a method that does allow for a quick translation between static and dynamic inference in the context of the prediction of fatigue lifetime is Kassapoglou's method for fatigue life of metal alloys [14]. Kassapoglou's method uses stress-strain data directly from static testing to predict fatigue lifetimes for a range of amplitudes and loading ratios. He uses the non-linearity in the static stress-strain curve to infer the plastic energy dissipated per loading cycle. The procedure involves fitting a Ramberg-Osgood type constitutive equation to the static stress-strain curve and using the non-linear relation (and a few additional geometric assumptions on the hysteresis loop) to calculate plastic energy dissipation for a given loading cycle (see Figure 2.3).

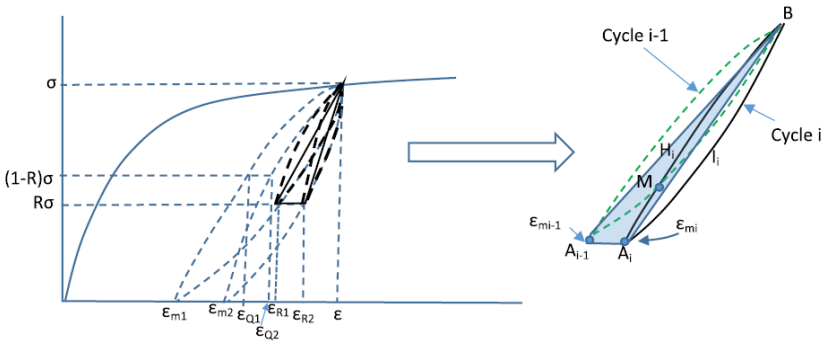

Figure 2.3: Kassapoglou's calculation of cyclic plastic hysteresis energy dissipation for $0 \leq R \leq 1$ ([14]).

The material lifetime can be predicted by calculating the number of cycles when the cumulative plastic strain energy dissipation reaches the total available strain energy density, represented by the total area under the stress-strain curve.
As mentioned in 2.1, composites exhibit a more complex fatigue behavior than metals. In terms of damage work, for example, when dealing with composites, it may be more accurate, on the macroscale, to speak of discrete and heterogeneous (damage) energy release events than of continuous plastic dissipation per loading cycle. Nevertheless, relating non-linearity in stress-strain measurements to progressive and irreversible cyclic energy release by damage events may provide an insightful and exciting new approach to fatigue modeling of FRCs.

2.1.2. Mechanical Damage Events

Mechanical micro-damage in composite materials can initiate within one of the components, leading to fiber breakage or matrix cracking, or at one of the interfaces: delamination, fiber-matrix debonding, interfacial shear failure/fiber sliding ([15], [16]). Delamination indicates a major damage type that involves the failure of the bond between two plies of the composite structural element. This happens in particular between plies of different orientation, where large out-of-plane shear effects can cause failure of the bonded interface. Fiber-matrix debonding happens when the resin detaches from the fiber, effectively isolating parts of the fiber from load transfer. Interfacial shear failure or fiber pull-out is another failure mode of the fiber-matrix interface, which also leads to unsuccessful load transfer between the fiber and the surrounding material, causing the fibers to slide out of the matrix. Physically, this damage mode may be regarded as a combination of fiber breakage and interfacial debonding.

Damage takes place due to stress concentrations, stress anisotropies, and shear effects that arise in the complex stress state during (multi-axial) loading, which is caused by the internal structural anisotropy of FRCs. According to Degrieck & Van Paepegem [11], the first cracks during tensile fatigue loading of cross-ply specimens are transverse through-thickness matrix cracks in the 90°-plies (perpendicular to the loading direction), which have the weakest longitudinal properties. The cracks in the matrix then spread to the plies of lower angle orientation.
In addition to the inhomogeneity of the intended design, undesirable manufacturing defects are present even in 'pristine' specimens. For manufacturing using vacuum infusion, these defects include voids, resin-rich areas, fiber misalignment or waviness, and regions where the resin has poorly wetted the fibers. When using a prepreg layup for the manufacturing of the laminate material, the main source of unintended manufacturing defects is the poor adhesion of the plies and inter-ply voids caused by air or moisture trapped between the layers of prepreg during manual layup. Suriani et al. [17] noted that damage initiates in these regions and eventually brings about the onset of structural failure in natural fiber-reinforced hybrid composites.
The progressive damage state of the material during fatigue loading can also exacerbate localized stress concentrations. The further development of damage is therefore accelerated as the specimen deteriorates under fatigue loading.

Damage initiates when the strain potential energy locally exceeds a threshold value due to the stress concentrations in the complex internal stress field. This threshold value depends on the material(s) and the observed damage mode. The excess strain potential energy is then irreversibly released in a burst event that marks a fiber fracture, a crack initiation, or a crack growth.
The released energy travels away from the source in different forms and dissipates over distance. It can be picked up by a variety of (passive) structural health monitoring techniques, such as passive infrared thermography (IRT) or acoustic emission (AE) monitoring. Passive IRT measures temperature changes in the material due to fatigue heating, i.e., the irreversible thermoelastic strain release caused by rapid damage formation. Zalameda & Winfree [18] were able to identify damage locations and size by picking up the transient thermal responses of the material during quasistatic and cyclic mechanical testing using an IRT camera. AE monitoring is covered in further detail in section 2.2.1.
The elastic energy, on the other hand, is redistributed onto the intact material. This redistribution of elastic strain energy can cause the overall mechanical properties of the composite structure to change compared to the pristine state, well before final failure is expected. An accurate model of fatigue of composite materials should capture and take this perceptible effect of global stiffness and strength degradation into account.

2.2. Structural Health Monitoring (SHM) and Non-Destructive Testing (NDT) Techniques for FRCs

Nondestructive testing (NDT) refers to the process of detecting and evaluating damage on both the surface and within the interior of materials without physically cutting, modifying, or damaging them. A variety of techniques are employed in the field of composite NDT, including Visual Inspection, Ultrasonic Testing (pulse echo ultrasonic method), Thermography Testing, Radiographic (X-Ray) Testing, Acoustic Emission, and Shearography Testing [19].
SHM techniques are NDT techniques that are used to monitor the damage/health state of structural elements *in situ* throughout their lifetime.

2.2.1. Acoustic Emission (AE) Monitoring

AE monitoring is a passive SHM technique that involves the measurement and analysis of the elastic waves emitted by damage events [19]. During a (micro-) damage event, the localized excess strain potential energy is transformed partly into local damage work, and partly into mechanical vibration and heat. The mechanical vibration causes the emanation of (elastic) stress waves that travel out concentrically and can be detected by an array of highly sensitive receptors.

In her review on non-destructive testing methods of composite materials, Gholizadeh [19] points out that AE monitoring can be used to identify and characterize the source of a recorded signal, a significant advantage over other passive NDT methods. She claims that the (frequency-) information carried by the wave can be used to differentiate between signal sources, i.e., different physical damage mechanisms such as fiber fractures, matrix micro-cracks, fiber-matrix debonding, and delamination. This claim is supported by extensive research that has been carried out on the topic in recent years ([20],[21],[22],[23]). Please refer to 2.3 for an overview of damage mode classification using AE waveforms.

In practice, AE monitoring involves an array of sensors that can detect the micro-displacements of the material due to the propagation of the elastic wave generated by the damage event [16]. The elastic oscillations can be picked up on the surface by surface-mounted piezoelectric sensors or by laser-based methods such as Laser Doppler Vibrometry.
Embedding sensors into the material is another option that may improve the sensitivity of damage detection. Huijer et al. ([24],[25]) proved the feasibility of embedding piezoelectric wafer sensors into a composite marine propeller blade. They were able to implement an SHM framework for *in situ* damage detection using embedded piezoelectric sensors that allow monitoring of damage without disrupting the propeller's operation in real-world applications.
Fiber optic sensors have been explored as an alternative to piezoelectric AE sensors for embedded monitoring. They have drawbacks compared to piezoelectric sensors in terms of detecting high-frequency displacements, but can be easily embedded without disrupting the fiber-array structure of FRCs [26].

2.2.2. X-ray Micro-Computed Tomography (Micro-CT)

Micro-CT has emerged as a highly effective *ex-situ* NDT method for the evaluation of FRCs [16]. This technique enables detailed scanning and characterization of internal material structures, offering insight into material heterogeneities, defects, and fiber distribution without damaging the specimen. The technique uses high-energy (X-ray) photons to create a 3D tomographic image of the internal structure of a scanned specimen.

In X-ray (micro-CT) tomography, the core workflow consists of the following steps:
First comes the measurement. As the X-ray source emits photons through the specimen, a detector (e.g., a flat-panel sensor) records how many photons arrive at each pixel. What's measured at each pixel is the transmitted intensity, ***I***, i.e., how many photons "make it through" along each ray path.
Then comes reconstruction. From the transmitted intensities, the system computes the line□integral of the attenuation coefficient μ along each ray, $\int \mu(x)dx$. A reconstruction algorithm (e.g., filtered back□projection or an iterative method) then "inverts" all of those line□integrals to produce a 3D map of local attenuation coefficients, $\mu(x, y, z)$. Finally, that μ-map is displayed as a grayscale image, where each voxel's brightness is proportional to its X-ray attenuation.
This is the reason why air looks dark and metal looks very bright: Almost all X-rays pass through air with minimal interaction. In other words, if a ray goes through "just air" before hitting the detector, its transmitted intensity ***I*** is almost equal to the incident intensity $\mathbf{I_0}$. Mathematically, because $\mu_{air} \approx 0$, the line integral $\int \mu_{air} dx \approx 0$. Reconstruction assigns a very low attenuation value to those voxels, and by convention, low-μ materials (like air) are displayed as dark (black) in the CT slice.
In contrast, metals have a very large attenuation coefficient μ_{metal}, and almost all X-rays get absorbed or scattered out of the primary beam. As a result, the transmitted intensity ***I*** reaching the detector is extremely small. During reconstruction, a small ***I*** (relative to $\mathbf{I_0}$) corresponds to a large value of $\int \mu(x)dx$. Voxels that contain (or lie behind) metal get assigned large μ-values, and appear bright (white).
The result of each micro-CT scan is a tomographic grayscale image representing matter density (i.e. photon absorption/beam attenuation) in 3D space.

In composite materials, the micro-CT will highlight material heterogeneity, both desired and undesired. In particular, fibers and matrix have different scattering properties and can, in theory, be differentiated in a

high-resolution scan. Material heterogeneity is present on multiple length-scales, and the resolution of the measurement determines the kinds that the scan will be able to detect. Identifying single broken fibers or first micro-cracks in the matrix during the initiation of fatigue deterioration probably requires a resolution in the order of a few microns ($5 - 10\mu m$) or less. Larger regions of coherent damage, voids, and resin-rich areas can be detected using lower resolutions.

As the resolution of a scan increases, the total scanned volume portion of material per scan becomes smaller. One of the challenges when working with Micro-CT is the vast amounts of data generated by every scan, so to keep the amount of raw data manageable, it is advisable to limit the scanning to a localized region of the specimen [27].
Nevertheless, Micro-CT offers a high-resolution insight into the structure of (a section of) the composite specimen at the meso- (and possibly micro-) scale, and can be considered a ground truth in terms of the damage state of the material. It can, in theory, detect all types of damage where a fracture leads to an interface detachment and plastic misalignment, making it a very useful tool to validate predicted damage in a small, localized region of composite material.

2.3. Damage Identification and Characterization using AE

When a sensor detects an AE hit, a waveform, among other properties in the time domain, can be stored. A hit is usually registered whenever the transduced signal crosses a certain threshold (often 40 dB).
In a post-processing step, properties in the frequency domain can be computed using a variety of transforms on the registered waveform. Two of the most prominent numerical techniques for generating frequency spectra from a time series are the fast Fourier transform (FFT) and the continuous wavelet transform (CWT) [22]. The registered waveforms are transient and multi-modal signals, which makes the CWT preferable over the FFT for computing frequency information. The drawback of the CWT is the increased computational effort compared to the very efficient FFT [22], and a limitation concerning frequency resolution for high frequencies that will be discussed further down in this Section.
Commonly observed features of the waveform are covered in section 2.3.1. Many of them have been used as inputs to a variety of (unsupervised) machine-learning algorithms to classify AE hits in categories related to specific damage modes. A few relevant instances of application of such methods are reported in Section 2.3.2.

2.3.1. Feature Selection

Feature extraction is the process of vectorizing observations by registering *d* pertinent features. Selecting these is the first challenge encountered when dealing with AE data analysis.

In general, properties of a hit, both in the time and frequency domains, have been used to differentiate damage mechanisms at the source of the AE. In the literature, there are many examples of characterizations of damage modes using different choices of observed features. According to Huguet [20], the following six parameters in the time domain are the most used in AE damage mode classification problems: rise time, number of counts, energy, duration, amplitude, and number of counts during the rise. Harizi et al. [23] chose 13 descriptors, both in the time and the frequency domain, to perform a multivariable statistical analysis: rise time, counts to peak, counts, duration, amplitude, energy, absolute energy, average frequency, ASL (Average Signal Level), RMS (Root Mean Square), reverberation frequency, initiation frequency and signal strength.

Although both time- and frequency-domain descriptors of AE signals can be used for damage mode classification, Muir et al. [22] suggest that there is a common agreement that features in the frequency domain are superior to features in the time domain. They state that ”there are encoded characteristics within the frequency domain of waveforms that relate AE to damage modes”.
Obtaining the frequency spectrum of an AE event is a question of post-processing the recorded waveform. The waveforms of AE events are non-stationary signals, which means that the frequency content is transient and changes over time. Common options to extract frequency information are the fast Fourier transform (FFT), continuous wavelet transform (CWT), wavelet packet transform (WPT), and empirical mode decomposition (EMD) [22]. Direct FFT returns one-dimensional frequency information in the form of an energy spectrum vector, and it is ill-suited for non-periodic, transient waves. CWT has an automatic windowing property that makes it suitable for analyzing non-stationary signals [28]. The CWT consists of a convolution of the signal $x(t)$ with a wavelet function $\psi(f, t)$ for different time-shifts t and -scales f

according to Eq. 2.1 (τ being the dummy variable of signal convolution along the time-axis):

$$CWT(f,t) = \int_{-\infty}^{\infty} x(\tau) \cdot \psi(f, \tau - t) d\tau \tag{2.1}$$

Popular wavelet functions ψ are the Morlet (see Figure 2.4) and the Daubechies wavelets. The CWT returns 2-dimensional time-frequency information in the form of a signal energy matrix.

In the following paragraph, the issue of the resolution of frequency spectra in the frequency domain is discussed, including an intuitive explanation of the Heisenberg Uncertainty Principle. Another popular method of time-frequency analysis (next to CWT) is the Short-Time Fourier Transform (STFT), which uses the Discrete-Time Fourier Transform (DTFT) on short sub-periods of the signal to get time-dependent frequency spectra. The length of the sub-periods can be varied, and the frequency resolution of the instantaneous spectra resulting from the DTFT on the sub-period is related to the Nyquist frequency and the number of samples included in the sub-period of the signal. The Nyquist frequency is the highest frequency that can be accurately represented in a discrete signal and is constant for a signal, equal to half of its sampling frequency, fs/2. Specifically, the resolution of the short-period frequency spectra is given by the sampling frequency (fs) divided by the number of samples (N): fs/N. This essentially means that the spectrum generated by DTFT has a constant top frequency of fs/2, and the resolution of the rest of the spectrum (between 0 and the Nyquist frequency fs/2) is given by fs/N, with N being the size of the time window. So, smaller N (i.e., smaller time window, i.e., higher time-resolution) gives a coarser frequency resolution, i.e., a larger fs/N.
This phenomenon is called the Heisenberg Uncertainty Principle, which states that there's a trade-off between time and frequency localization. It is explained conceptually by the fact that neighboring frequencies only go out of phase and cancel out after a large number of cycles. Therefore, to catch fine differences in the frequency contents of a signal, many cycles, i.e., long periods in time, must be included. A lemma of this principle is that frequency contributions with low cycle counts (e.g., high-frequency contributions of short durations) can never be identified with a high resolution (because it would require a high resolution in time and frequency combined, which is impossible).
This principle applies in general, and therefore to the method of CWT as well. In this case, it manifests in the fact that the frequency content (i.e., the Fourier transform) of the Morlet wavelet itself is narrow-banded for large σ (i.e., low frequencies) and broader for high-frequency wavelets. This leads to a worse resolution in the frequency domain, as it captures a broader band of frequency contributions.

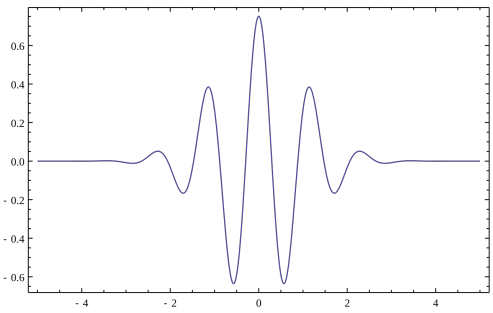

Figure 2.4: Real-valued Morlet wavelet $\psi(t) = \mathcal{R}e\{e^{2j\pi ft}e^{\frac{-t^2}{2\sigma}}\}$, with $\sigma = \frac{n}{2\pi f}$, and n umber of cycles included in the wavelet. [29].

Returning to the frequency spectra of acoustic emissions in composite materials, Muir et al. [22] point out that energy contents at specific frequencies can depend not only on the type of source but also on propagation pathways. Therefore, values at a single frequency alone should not be used for the characterization of the signal's source. The authors suggest instead the option to analyze patterns in the frequency domain or the overall frequency spectrum to accurately link AE signals to damage modes.

Kempf et al. state that the "entire frequency composition of an AE signal is characteristic for the underlying failure mechanism" [21]. They perform static tensile testing on glass fiber-reinforced polyurethane specimens while recording AE and identify frequency spectra associated with matrix cracking, interphase failure, and fiber breakage. The average spectra are reported in Figure 2.5. The sensors used in that

study were two wideband WD-sensors with a bandwidth of 100–1000 kHz. They show sensitivity peaks at around 270 kHz, 410 kHz, and 530 kHz, which are reflected in the spectra in Figure 2.5. The signals were grouped into three classes based on a feature clustering algorithm (including the following features: peak frequency f_{peak}, weighted peak frequency $f_{WPF} = \sqrt{f_{peak} \cdot f_{centroid}}$, and partial energy of the frequency spectra in low- $(0 - 250kHz)$, mid- $(250 - 450kHz)$, and high-frequency range $(450 - 800kHz)$). Weighted peak frequency is significant to capture both peak sharpness and spectral center at the same time. The three clusters were subsequently assigned to a class of damage by assuming that matrix cracking emits AEs of lower frequencies, whereas fiber breakage emits AEs of higher frequencies. Interphase failure was assumed to cause AEs with frequency contributions in the middle range.

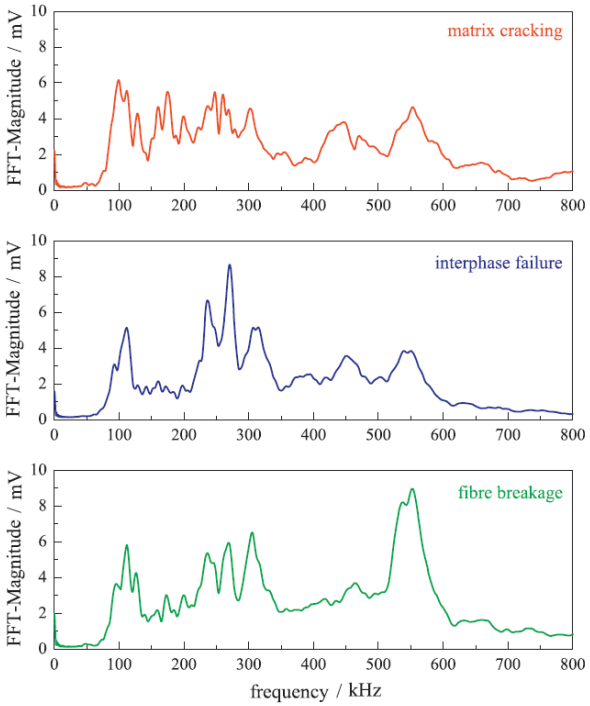

Figure 2.5: Average FFT spectra of matrix cracking, interphase failure, and fiber breakage in glass fiber reinforced polyurethane as identified by Kempf et al. [21]

Finally, Kempf et al. used a post-mortem scanning electron microscopy (SEM) fracture surface micrograph to highlight that for one sample, the one for which fewer AE hits had been registered before final failure during testing, the interface between matrix and fibers seemed to have snatched right off during final failure, whereas for the other one the degradation of the interface had seemingly been more gradual. The study provided initial insights, though it lacked extensive experimental validation of the robustness of classification.

It is generally accepted that fiber fracture has the largest contribution in the high-frequency range due to the higher modulus of elasticity of the fibers, and the energy spectrum of matrix cracking is more skewed to the left, towards lower frequencies [30]. AEs generated by fiber-matrix interfacial failure are assumed to have signals in the mid-frequency range. Qiao et al. [31] used frequency bands of the main energy distribution of the registered waveforms (62.5–125 kHz) (125–187.5 kHz), (187.5–250 kHz), (250–312.5 kHz) and (312.5–375 kHz) to recognize four types of signals corresponding to matrix cracking, delamination, fiber/matrix debonding and fiber breakage repsectively. They used pre-cracked and untreated specimens to controllably favor different kinds of damage modes during a three-point bending test and subsequently compared the classification results of their novel machine learning (ML) approach (using support vector machines (SVMs)) to the more conventional k-means clustering, achieving similar accuracy. Again, no extensive validation campaign was conducted in this context to validate the classification of the registered signals empirically.

2.3.2. Unsupervised Machine Learning Techniques

Once the pertinent signal features (in the time or frequency domain) are chosen, the AE data can be uniformly represented. The next challenge is to identify structures within this data that allow the differentiation between damage modes. Machine Learning (ML) is a set of powerful algorithms that learn from input data and can uncover naturally occurring structures. Supervised ML can be used to train a classification model if a large set of labeled feature data is already available. Popular examples of this include regression algorithms and neural network training.
In the case of AE, it is very difficult to obtain labeled AE data, i.e., AE data differentiated in advance by damage modes. For this reason, another approach of blind labeling or 'unsupervised' ML is more suitable. Two of the most common types of unsupervised ML algorithms are clustering algorithms and dimensionality reduction techniques ([22], [32], [31], [33]).

Dimensionality Reduction

Principal Component Analysis (PCA) is an unsupervised ML method from the field of multivariate data analysis that returns the principal components of a dataset [34]. The principal components (PCs) or 'modes' of the data are the (orthogonal, i.e., non-redundant) directions of largest variance from the mean feature vector and are ordered in ascending order. The order of a principal component is a measure of the variation of the data in that direction. The first PC describes the direction of maximum variance of the data from the mean, the second denotes the direction of largest remaining variance, and so on [28]. In simpler terms, PCA finds the most meaningful directions in the data along which AE features vary the most. It follows that representing AE datasets in the space of the first two or three principal directions may spatially separate and visibly highlight qualitatively different subgroups of data points in the dataset.

PCA is performed by finding the eigenvectors of the (mean-subtracted) dataset's covariance matrix or, more efficiently and stably, by performing a singular value decomposition (SVD) directly on the (mean-subtracted) dataset. Implementations of the technique exist for most programming languages and return an orthonormal basis of the feature vector space. The Eckart-Young-Mirsky theorem guarantees that the truncated SVD finds the best-possible low-rank approximation, i.e., the orthogonal projection into a lower-dimensional subspace that minimizes the squared reconstruction error [35].
For this reason, PCA is a valid method of reducing the dimensionality of the AE data without losing the features that are most significant for the differentiation of the signals. This explains why PCA is a popular technique in studies using automatic pattern recognition for blind AE source identification, because it highlights characteristic compositions of features that point to qualitatively different points in the data ([32], [33]).

Baccar & Söffker [28] used PCA to identify the first two dominant spectral components of each AE hit in their AE dataset. They applied CWT to generate the energy matrix from the waveforms consisting of 1000 time samples. Thus, they generated a set of 1000 frequency spectra for each hit. Then, they repeatedly used PCA on each of these sets separately and identified for each the first two principal components. They further used these as input for their classification scheme. This reduced the stored frequency data for each hit from 64,000 (64 x 1000) to 128 (64 x 2) values. A running algorithm that reduces the amount of stored data without losing relevant information can be of great advantage, especially during fatigue tests, throughout which vast amounts of AE data are generated.

Clustering Algorithms

Once the data is 'spatially' separated into directions of largest variance from the mean vector with the help of PCA (even using 2 or 3 coordinates only), it can be categorized blindly using clustering algorithms with improved accuracy. Clustering algorithms are useful to group data points into several 'clusters' such that each cluster contains points that are close to each other in the given metric space. Muir et al. [22] mention two unsupervised classification (or clustering) algorithms that are used in the context of AE data processing: K-means and Gaussian mixture models (GMMs).

K-means finds *k* spherical clusters in the feature space according to a distance norm, usually L_2. This makes it particularly suited for differentiating convex and well-separated regions of data point density [36]. K-means is a hard clustering type of method.
A popular example of a soft clustering method, on the other hand, is the fuzzy C-means algorithm [37]. Instead of assigning a distance-based cluster membership to each data point (like K-means), fuzzy C-means assigns to each data point distance-based membership values (between 0 and 1) for each cluster.

This means that it allows partial membership to multiple clusters, which is an advantage when dealing with partially overlapping clusters or when data points do not fit neatly into one cluster.

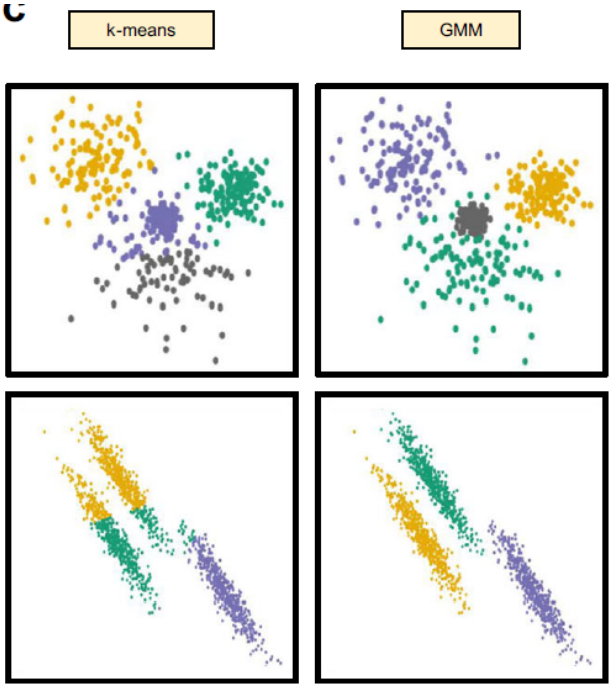

Figure 2.6: The performance of a generic k-means (left) and GMM (right) algorithm on a sample 2D isotropic (top row) and anisotropic (bottom row) Gaussian data set to show GMM's improved performance in recognizing naturally occurring Gaussian data distributions ([22]).

GMMs are an alternative to K-means, which allows for soft, probabilistic clustering. They offer an advantage in representing anisotropic data clusters in the feature space, and there is reason to suspect that this is beneficial in the context of AE data classification in many feature spaces [32]. The GMM algorithm finds *k* multivariate Gaussian distributions (fully characterized by two parameters: mean feature vector μ and covariance matrix Σ), such that the training data is optimally represented by their probabilistic distributions. After the GMM has been trained, a new data point can be classified into one of the *k* clusters. The probabilities of generation can be calculated using the Gaussian distribution of each cluster, and the new point will be assigned to the cluster with the highest probability of generation. GMM is also an example of soft clustering, i.e., each data point belongs to all clusters with varying degrees of membership. Moreover, it is a probabilistic clustering method that assumes that Gaussian distributions are underlying the generation of the data. Therefore, it performs particularly well when the data is naturally Gaussian distributed (around a mean with an elliptic variance).
Sample performances of k-means and GMM are demonstrated on dummy Gaussian data sets in Figure 2.6.

2.4. Knowledge Gap

Returning to Talreja's findings in Figure 2.2, note that fatigue failures of unidirectional composites in Region II are caused by fatigue of the fibers or (prematurely) by a progressive degradation of the matrix, which results in stress concentrations, redistribution, and parts of the structural material becoming isolated from the load due to growing and cumulating cracks. This is a gradual and discrete-event process that manifests in acoustic emissions during loading cycles.

A standardized methodology for the identification of damage modes in FRCs using AE signals is still lacking. In many cases, the classification of AE events includes information about signal amplitude and energy content, but a promising alternative is to identify damage modes using normalized frequency information only. Here, opinions diverge as to which is the best way to extract frequency information from

registered signals (FFT, CWT, WPT, Hilbert-Huang transform, [22]), and how to handle that frequency information. In the current research, an approach is proposed to extract the frequency content of an AE wave packet and to characterize the physical damage mode at the source of an AE event without taking into account the energy content of the signal.
AE classification typically lacks physical validation, so, in this study, the classification of the normalized frequency spectra shall undergo a targeted validation campaign using X-ray Micro-CT scanning. This technique can be used to create high-resolution snapshots of the internal structure of the specimen before and after mechanical loading. These can, in theory, be used to assess the evolution of damage during mechanical loading and support or refute the predictions made by the AE monitoring framework.

Please refer to Chapter 4 for further details on the developed methodology.

3

Research Questions (RQs)

Literature says that micro-structural damage events can be located in the material and differentiated by type of damage using acoustic emission (AE) monitoring. Based on findings in the reviewed literature (in particular [22],[21],[31]) and the identified knowledge gap, the need is recognized to assess the feasibility of an acoustic emission (AE) monitoring framework capable of tracking the local evolution of damage in composite materials while distinguishing between different damage modes, and of validating said monitoring framework using a high-fidelity method such as X-ray micro-CT scanning. The following research questions and sub-questions can thus be formulated:

(I) How can damage events in composite materials be detected and accurately characterized using the entire shape of the normalized frequency spectra (in a relevant range) and the energy contents of the corresponding AE signals independently?

- **(I.a)** What is an effective method of extracting frequency information from registered AE signals, so that the impacts of background noise and reflections at the specimen's boundaries are reduced and the specificity of the frequency content (related to the source of the signal) is increased?
- **(I.b)** How can the normalized frequency spectra of AE events be classified into a finite set of families based on the similarity of their shapes? Moreover, do AE events have characteristic frequency contents that are comparable between different transducers (of the same type) located at different positions along the specimens?
- **(I.c)** Do different families of AE spectra correlate with the physical damage states observable in high-resolution micro-CT scans (fiber fracture, inter-fiber or transverse matrix cracking, fiber-matrix interface failure, and delamination)? In particular, can a family of frequency spectra be identified that uniquely corresponds to fiber fracture events (for transducers of a given type)?

(II) Can X-ray micro-computed tomography (micro-CT) be used to validate the AE monitoring framework elaborated in the scope of RQs (I.a-c) by allowing to visualize and track the development of micro-structural damage in unidirectional fiber-reinforced composite coupon specimens?

- **(II.a)** Are tomographic images that are recorded before and after the infliction of damage comparable using basic image processing techniques or visual inspection, and can this comparison be used to assess what kind of damage event took place?
- **(II.b)** What is the highest attainable resolution of the micro-CT image, and is it high enough to reveal micro-damage (such as (single) fiber fractures, initiating and growing inter-fiber or longitudinal matrix cracks, and fiber-matrix debonds)?

4

Methodology

In the following, an AE monitoring setup (with related data processing, and analysis methods) and a series of tomographic imaging and mechanical tests are proposed to answer the RQs **I** and **II** in Chapter 3 using a batch of unidirectional carbon fiber reinforced composite (CFRC) coupon specimens.

4.1. Materials and Specimen Preparation

A batch of twelve unidirectional CFRC coupon specimens has been manufactured in the context of this work from a carbon-fiber-epoxy-resin-prepreg system for out-of-autoclave (OOA) curing (TORAY Composites 2510 Prepreg System, data sheet in [38]). Relevant material properties used in the context of this work are given in Table 4.1. The assumption $G_{13} \approx G_{12}$ is made because transversely isotropic behavior is assumed for the unidirectional laminate. This is a reasonable assumption, although in reality they might differ due to manufacturing defects, in particular at the interface between the plies of prepreg, and non-uniform scaling of the material properties in different dimensions.

Material Property	Symbol	Value [38]
0° Tensile Strength	F_{1t}	$2172\,\text{MPa}$
0° Tensile Modulus	E_{1t}	$125\,\text{GPa}$
0° Compressive Modulus	E_{1c}	$112\,\text{GPa}$
In-Plane Shear Modulus	G_{12}	$4.23\,\text{GPa}$
(Out-of-Plane Shear Modulus)	(G_{13})	($4.23\,\text{GPa}$)
Poisson's Ratio	ν_{12}	0.31
Laminate Density	ρ	$1517\,\text{kg/m}^3$
Fiber Volume Fraction	V_f	54.4%
Cured Ply Thickness	CPT	$0.152\,\text{mm}$

Table 4.1: Selected mechanical properties of the cured unidirectional (carbon-fiber-epoxy) laminate (P707AG-15) at 22°C ambient temperature. Note that the assumption $G_{13} \approx G_{12}$ has been made.

The design of the specimens is based on the ASTM D3039 [39]/ISO 527-5 [40] standards for unidirectional 0°-laminate for tensile experiments. A slight deviation from the standards is the specimen width of 20 mm, which was introduced to ensure the successful mounting and bonding of the AE transducers onto the specimens (compare [21]). The standard and the custom dimensions for specimens and end tabs are shown in Table 4.2 and Figure 4.1.

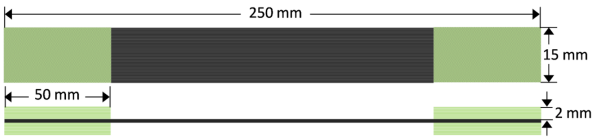

Figure 4.1: Standard specimen and end tab dimensions [41]

	ASTM D3039 [39] / **ISO 527-5** [40]	Used in this study
Width	15 mm	20 mm
laminate Thickness	1 mm	1 mm
total specimen Length	250 mm	250 mm
End Tabs	chamfered (7°-90°), rectangular	straight (90°), rectangular

Table 4.2: Design standards for unidirectional 0°-laminate tensile coupon specimen ([39], [40]) and custom dimensions used in this study.

The end tabs were glued onto the specimens using epoxy adhesive (EA3430) to protect the clamped ends from surface damage due to the compressive traction grip of the mechanical testing rig during the application of mechanical loading. Moreover, they can relieve stress concentrations that would cause premature failure at the clamped end, well before the gauge length of the specimen fails [41]. Aluminum end tabs were used in this study as they are the most common and readily available option. Woven or [45°] glass-fiber end tabs may be preferred when testing specimens up to higher loads.

The specimens were manufactured by applying the desired layup and carrying out the OOA curing of a 300 mm by 300 mm unidirectional carbon fiber plate of 1 mm thickness. The plate was subsequently machined into twelve specimens of the desired dimensions. The desired layup consists of six unidirectional plies of 0.152 mm in longitudinal direction ($[0°]_6$), amounting to a total thickness of 1 mm.

4.2. Tools and Equipment

The following paragraphs detail the machines, tools, and equipment used in the experimental campaign.

4.2.1. Tensile Testing Machines

In the current work, two specimens ('U7' and 'U9'), out of the twelve that have been manufactured according to 4.1, have been tested under tensile loading to induce internal damage while monitoring acoustic emissions using a *20 kN* (specimen U7) and a *Zwick 250 kN* Universal Test Machine (specimen U9). Note that both machines are displacement-controlled and load is transferred to the specimens by traction grips that press into the specimen end tabs and are controlled hydraulically (in the case of the *250 kN* Test Machine) or mechanically (*20 kN* Test Machine). Mechanical clamps (used for specimen U7) are set manually to a defined clamping pressure at the beginning of the experiment and then remain fixed throughout the tensile experiment. This may result in a drop in traction force and premature termination of the experiment as the specimen elongates during tensile loading and consequently contracts in the through-thickness direction due to its positive Poisson ratio. Hydraulically controlled grips (used for specimen U9) are capable of tightening automatically as the specimen contracts under tensile loading. This way, clamping pressure can be kept constant during the experiment, which can help prevent specimen slippage and premature termination due to the loss of traction.
For accurate strain measurements, there is the option of adding an extensometer to the testing setups. The extensometer pin heads attach to the specimen at an initial gauge length of 50 mm and follow the elongation of the specimen, giving an accurate value for the theoretically uniform internal strain of the unidirectional specimen. Strain measurements using an extensometer were included while testing specimen U7 on the 20 kN testing machine, but when testing U9 on the 250 kN machine, the extensometer was out of service due to technical issues in the data collection motherboard.

4.2.2. Micro-CT scanner

The Micro-CT scanner used to visualize the internal microstructure of the material before and after mechanical testing is the TESCAN, CoreTOM Micro CT, which theoretically allows for a volumetric resolution of up to 3 μm. However, the maximum attainable resolution depends on the diameter/width dimension of the scanned object, because the machine uses a flat panel detector with a resolution of 2856 by 2856 pixels. This means that for the given specimen width of *20 mm*, the top constraining resolution of a scan covering the entire width is $20mm/2856 \approx 7\mu m$. Achieving a top-resolution scan of high quality that covers the whole width of the specimen requires skill and expertise to align the object and the X-ray cathode with extreme precision.

4.2.3. AE Monitoring Setup

Acoustic emissions (AE) were monitored during the quasi-static tensile tests using externally mounted piezoelectric sensors. Similarly to Huijer's testing campaign [24], two transducers were mounted on the specimens to allow for the redundant identification of damage and to localize the events by triangulating the sources of the signals using the time difference of arrival (TDOA) method (see Section 4.4.1 covering the TDOA method). The ultrasonic signals of interest originating from micro-structural damage are in a measurable frequency range of 100 kHz to 1 MHz [21]. In the scope of this work, commercial surface-mounted white-band sensors shall be used for increased spectral sensitivity and setup reproducibility, namely the WSα $(100 - 1\,000kHz)$ wide-band AE sensors by MISTRAS Group. The transducers were mounted on the specimen using manual mechanical clamps that pressed into the top of the transducer and the back of the rectangular specimen (see Figure 4.2). A thin layer of grease was applied between the surface of the transducers and the specimen to create an acoustically transparent interface.

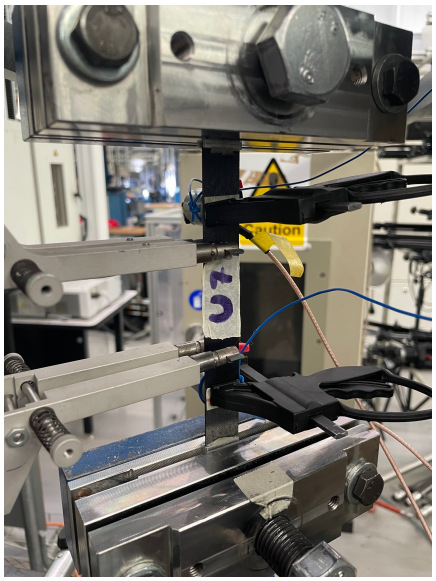

Figure 4.2: Specimen U7 mounted in the tensile testing rig. AE trasducers are clamped onto the back of the specimen using (black) manual clamps. The extensometer had locked onto the specimen for accurate strain measurement.

For the data acquisition (DAQ) *Vallen Systeme*'s multi-channel AMSY-6 system and the corresponding AE Suite software have been used (software documentation in [42]). This system identifies AE hits by registering threshold crossings of the voltage recorded by the previously described transducers (corresponding, in this case, to a threshold of 25.3 dB). A hit starts when the threshold is first crossed, and it's concluded when no threshold crossing occurs for a period called the 'rearm time' [42]. After a threshold crossing, once the rearm time has expired, a new hit is registered when the threshold is crossed once again. Hence, hits are differentiated by the period of 'silence' between them, when this period exceeds the amount of the 'rearm time' parameter.
In the context of this work, a rearm time of $100\mu s$ has been chosen to enhance and favor sensitivity of the AE monitoring framework in relation to successive events. Reflections, i.e. wave group packets that are reflected the ends of the specimens, are predicted to reach the transducers while the original hit is still being recorded (within $90\mu s$ of the arrival time of the primary wave packet), i.e. when the rearm time has not yet passed. It is undesirable to use a waveform that contains reflections in the analysis step, instead one would prefer to use only the 'clean' primary wave packet signal Ψ in this context. One could achieve a clean signal by reducing the rearm time, but this would also cause more hits to be recorded than intended, because reflections would cause additional hits at the transducers. A post-processing step is necessary to select only the duration of the first significant wave packet Ψ (with a duration $\leq 100\mu s$) from the recorded waveform. Increasing the rearm time may have an advantage in terms of reducing the number of AE hits caused by boundary reflections, but it may also reduce the sensitivity to successive hits that happen in a short period of time. Improving the choice of the rearm time parameter shall be the subject of further proposed work.

4.3. Experimental Procedure

This section covers the implementation and testing of the AE-based damage characterization framework and the validation thereof using Micro-CT scanning on the specimens detailed in 4.1. The execution of the experimental campaign involved the following three steps:

- High-resolution micro-CT scanning (with a resolution of $8\mu m$) of 'pristine' specimens in two different locations along the intra-sensor distance.
- Static tensile loading while monitoring AEs using two surface-mounted transducers aiming to induce and detect the creation and growth of internal damage.
- High-resolution Micro-CT scanning of damaged specimens in the same locations along the intra-sensor distance to validate the AE-based damage mode recognition framework.

It is crucial to limit damage in the observed regions to a few significant events. If too much damage develops in the specimen during mechanical testing, it will be difficult to assess if individual events are being characterized correctly by their type, or if just a general state of damage is being detected by the AE monitoring framework. For this reason, it is important to have the localization and characterization frameworks running before the start of mechanical testing. The specimen shall then be loaded carefully in stages of gradually increasing load. Once a few AE events have been recorded, the increase of mechanical load will be arrested to assess the development of damage in the regions of interest using the recorded AE data. Based on that, it will be decided whether to continue increasing the load or to stop mechanical testing, dismantle the AE monitoring setup, and get the specimen scanned for a second time.
Once the (now damaged) specimen has been scanned for the second time, the experiment is considered terminated for the specimen in question. If testing is to continue using the same specimen, it must be taken into account that the exact monitoring conditions are difficult to reproduce once the monitoring setup has been taken apart. Therefore, a second round of damage caused by tensile loading should be considered as an entirely new AE experiment with the second CT scan as the starting condition.

4.4. Data Collection and Analysis

This section covers the collection and analysis of the data generated by structural health monitoring using acoustic emissions (Subsection 4.4.1) and non-destructive testing using micro-CT (Subsection 4.4.2). It outlines the methods used to extract meaningful features from the raw signals and tomographic scans. The goal is to enable damage characterization and validate the AE-based classification framework.

4.4.1. AE Monitoring Framework

As detailed in Section 2.1.2, mechanical damage events can emit high-frequency elastic waves that travel away from the source and can be registered by the proposed AE monitoring framework. The surface-mounted PZT sensors are able to pick up out-of-plane elastic waves traveling through the specimen, and a digital filter of $40\,\text{kHz} - 960\,\text{kHz}$ is applied by the DAQ system directly to ensure that low-frequency elastic deformations or noise are not registered as additional hits or damage events.

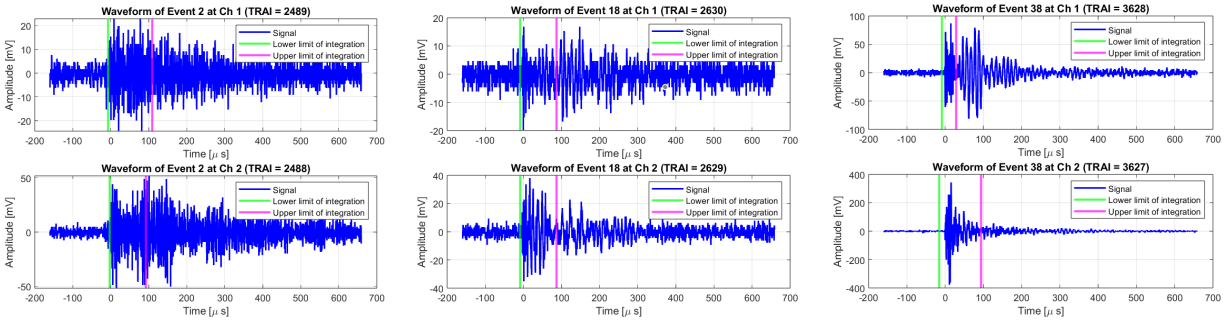

(a) Event 2 ($x = 151\,\text{mm}$) **(b)** Event 18 ($x = 155\,\text{mm}$) **(c)** Event 38 ($x = 151\,\text{mm}$)

Figure 4.3: Waveforms recorded by transducers 1 (above) and 2 (below) for three sample events located in the quarter-length region of validation ($138\,\text{mm} - 156\,\text{mm}$) of specimen U9.

When a hit is stored, baseline information includes the time of arrival, the channel, and the threshold of detection ($25.3\,$dB). Furthermore, *Vallen Systeme*'s DAQ system can save a range of AE feature data to a primary data file (PRImary Data Base, PRIDB), which prominently includes burst signal peak amplitude, burst signal energy, burst signal duration, ring down counts, and burst signal risetime [42]. The signal of a hit is sampled and the waveform stored to a transient data file (TRADB), with a sampling frequency of $2.5\,$MHz and with a fixed length of 4096 sample points per waveform. The waveforms registered by the two transducers for three sample events are shown in Figure 4.3.

Source Localization using Time Difference of Arrival (TDOA)
An AE 'event' is defined as an elastic wave that arrives at both transducers within a short time window ($\Delta t \leq 30\,\mu$s) and is registered as a pair of transient waveforms $\Psi_{total}(t)$ (one for each sensor). Events are localized using TDOA, which makes use of the time of arrival of the signal at the transducers and knowledge about the group velocity of elastic waves in the material to locate the source. When a long rectangular unidirectional fiber-reinforced composite specimen is monitored using two transducers, the location of the source along the length of the specimen x_{source} can be estimated according to Equation 4.1 using the longitudinal speed of sound v_g (along the direction of the fibers) and the time difference of arrival of the signal at the two sensors Δt [43].

$$x_{source} = \frac{\Delta t \cdot v_g}{2} \tag{4.1}$$

TDOA is sensitive to the input parameters, and the accuracy is limited by the time of arrival measured by the DAQ system and the longitudinal group speed of out-of-plane elastic waves. The time of arrival is defined as the time of the first threshold crossing of the event's signals at the respective transducer [43].

$$c_{p,S0} = \sqrt{\frac{A_{11}}{I_0}} = \sqrt{\frac{E_1}{\rho}} = 8838.3\,\text{m/s}, \qquad c_{g,S0} = c_{p,S0}, \qquad \text{where } E_1 = \frac{E_{1t} + E_{1c}}{2} \tag{4.2}$$

S0 is the fastest and hence the first wave mode to arrive at the transducers; however, the flexural (A0) mode usually causes the excursions of highest amplitude in the measured signal. This can be attributed to the different natures of the two types of elastic deformations and how they are transferred to the PZT transducer: the bending deformation (A0) causes an oscillation of higher amplitude at the contact surface of the sensor than the axial deformations of the S0 mode. Therefore, a large amount of useful signal information travels with the A0 mode, i.e., at lower speeds. This wave mode is dispersive and, therefore, requires detailed analytical or semi-numerical studies to estimate phase and group velocities. In the context of this work, exact values for the two velocities of the A0 mode are not essential for analysis and will therefore be replaced by an estimation of their high-frequency limits. In the limit of high frequencies, the phase velocity of the A0 mode $v_{p,A0}$ approaches the shear wave speed v_s (see formula in Equation 4.3), and the group velocity $v_{g,A0}$ approaches a limiting value close to shear wave speed, but not exactly equal because of residual dispersive effects and the effect of specimen geometry.

$$v_s = \sqrt{\frac{G_{13}}{\rho}} = 1669.8\,\text{m/s} \qquad v_{p,A0,lim} = v_s \approx v_{g,A0,lim} \tag{4.3}$$

The limiting group velocity of the A0 mode $v_{g,A0,lim}$ will become useful at a later stage in section 4.4.1, where it will be used to estimate an interval of the registered waveform containing the 'clean' signal, which can be used to generate frequency spectra.

Pencil Lead Break (PLB) Tests
A pencil lead break (PLB) test is a simple and widely used method in AE testing to simulate a localized and repeatable mechanical event (like a crack initiation) on the material's surface. The test involves breaking the tip of a pencil lead (usually 0.3 mm or 0.5 mm diameter, 2H or HB hardness) against a solid surface to create an acoustic signal (in the range of $100\,$kHz).
Three PLBs have been performed for each monitored specimen in three locations on the intra-sensor length ($x = 100,\ 125,\ 150\,$mm) as shown in Figure 4.4.

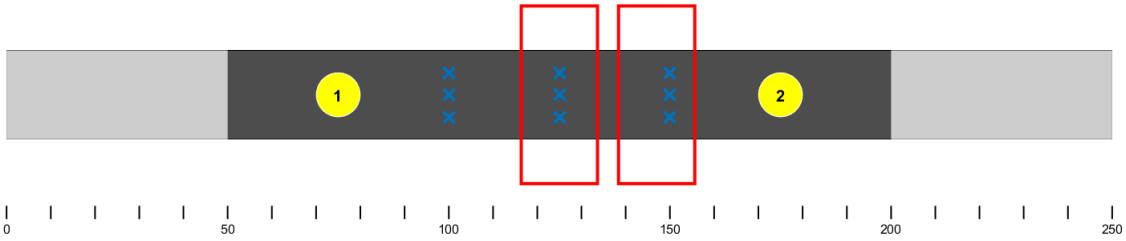

Figure 4.4: Locations of the PLB Tests performed on the monitored specimens U7 and U9. PLB locations are marked as blue crosses, sensor locations as yellow circles, and scanned regions as red rectangles.

The first objective of the PLB tests in this context is to validate the theoretical group speed of elastic wave packets $v_{g,S0} = 8838.3\,$m/s and the localization method using TDOA. The theoretical speed of guided waves along the longitudinal direction of the unidirectional FRC coupon specimens can be validated by performing PLBs at different locations along the intra-sensor section of the specimen (e.g., at 1/4 and 3/4 of the section) and measuring the time difference of arrival between the two sensors using the time of arrival of the wave packet.
PLB testing also has another purpose: In general, AE measurements are dependent on the sensors and the sensor-specimen transmission interface. So the measured energy content of the acoustic emissions generated by PLBs could be used at a later stage to compare signal energy contents across different transducers and monitoring setups.

Generating (Normalized) Wave Packet Spectra
Using a continuous wavelet transform (CWT, see Section 2.3.1) with a Morlet wavelet on the waveform signals $x(t)$ returns instantaneous frequency spectra in the form of matrices whose entries represent the energy of the signal at a given frequency and time. Figure 4.5 shows the CWTs of the six sample waveforms from Figure 4.3.

Integrating the wavelet spectra over all frequencies (Eq. 4.4) gives a representative value of the total instantaneous energy content of the signal over all frequencies at a given time. The instantaneous energy contents of the three sample events from Figure 4.3 are plotted in Figure 4.6 for channels 1 and 2.

$$E(t) = \int_0^\infty |CWT(f,t)|^2 df \tag{4.4}$$

Integrating the CWT over a time interval (Eq. 4.5), on the other hand, gives a vector whose components represent the energy at given frequencies contained in the chosen interval of the waveform.

$$S_\Psi(f) = \int_{T_{\Psi 1}}^{T_{\Psi 2}} |CWT(f,\tau)|^2 d\tau \tag{4.5}$$

The normalized frequency spectrum $\hat{S}_\Psi$ will be the normalized version of the vector S_Ψ, i.e., divided by the nominal energy content of the corresponding waveform (see Eq. 4.6).

$$\hat{S}_\Psi(f) = \frac{S_\Psi(f)}{E_\Psi}, \qquad E_\Psi = \int_{T_{\Psi 1}}^{T_{\Psi 2}} |x(\tau)|^2 d\tau = \int_{T_{\Psi 1}}^{T_{\Psi 2}} |\Psi(\tau)|^2 d\tau \tag{4.6}$$

Computing the integral (4.5) over the desired interval and normalizing according to (4.6) results in the six frequency spectra reported in Figure 4.7 for the three sample events from Figure 4.3.

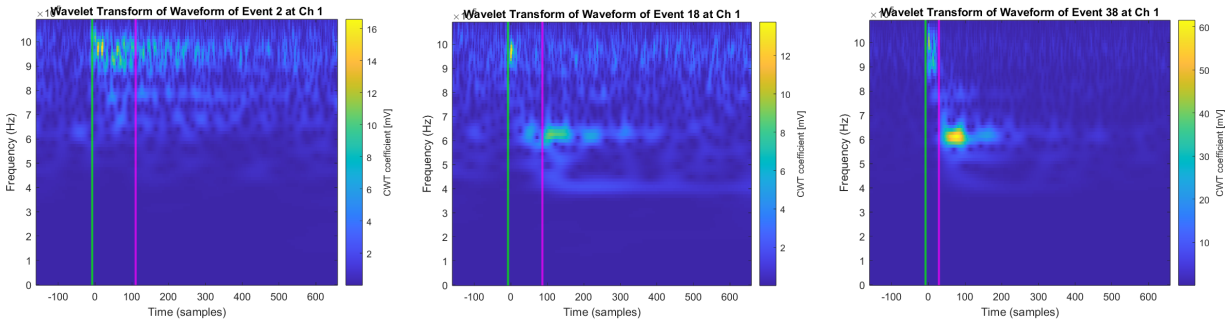

(a) Event 2, Ch 1 **(b)** Event 18, Ch 1 **(c)** Event 38, Ch 1

(d) Event 2, Ch 2 **(e)** Event 18, Ch 2 **(f)** Event 38, Ch 2

Figure 4.5: CWTs of sample waveforms recorded by transducers 1 (top row) and 2 (bottom row).

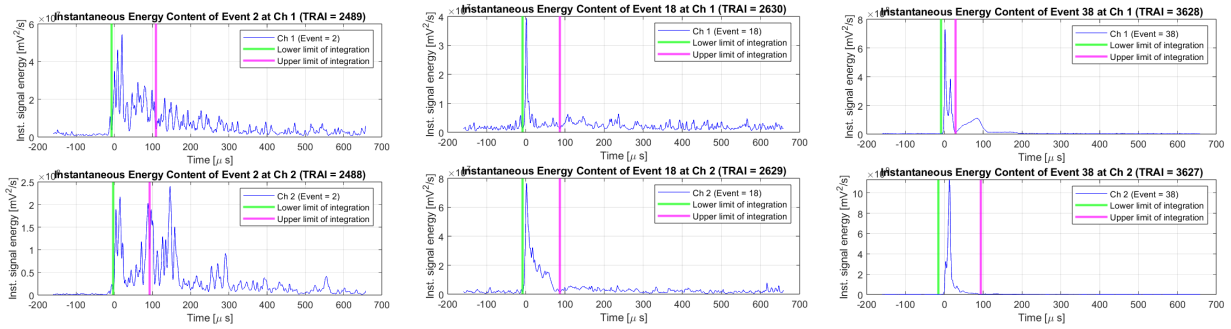

(a) Event 2 **(b)** Event 18 **(c)** Event 38

Figure 4.6: Instantaneous energy contents $E(t)$ of sample waveforms recorded by transducers 1 (above) and 2 (below). Vertical lines indicate the boundaries of the observed wave packet.

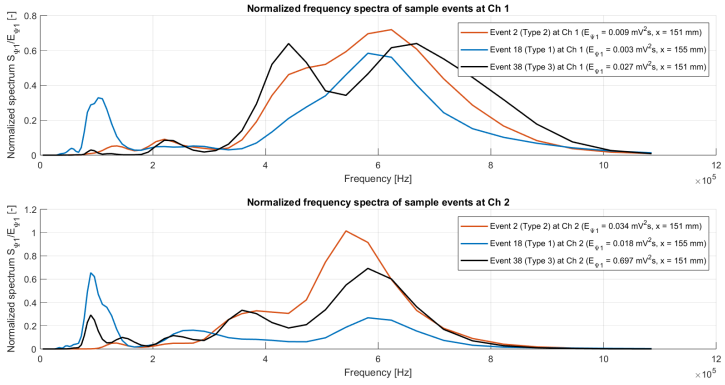

Figure 4.7: Normalized frequency spectra $\hat{S}_\Psi(f)$ of the waveforms recorded by transducers 1 (above) and 2 (below) on specimen U9 for sample events 2, 18, and 38.

How to choose the time interval over which to integrate the CWT (i.e. the two vertical lines in Figures 4.3, 4.5, and 4.6) to capture the frequency content of the full wave packet Ψ but avoid reflections is a pertinent question that will be answered in the following paragraph.
$\Psi(t)$ is the section of the total waveform $x(t)$ representing the 'clean' primary wave packet, excluding reflections from the boundaries of the specimen. The frequency spectrum of the wave packet $S_\Psi(f)$ is the time-integral of the CWT of the waveform over the interval containing Ψ.

The lower bound of the integral $T_{\Psi 1}$ is determined as the first local minimum of the (smoothed) instantaneous energy content of the waveform preceding the time of arrival of the signal $TThr$. The upper bound of the integral $T_{\Psi 2}$ is determined as the first local minimum of the (smoothed) instantaneous energy content of the waveform preceding the first estimated time of arrival of reflections from the boundary of the specimen of the A0 mode of the wave. Assuming that the instant of maximum instantaneous energy content $(t_{max}|E(t_{max}) = E_{max})$ of the waveform coincides with the time of arrival of the A0 mode, reflections are not expected to arrive at the transducer before a time period of $T_\Psi = 89.8\,\mu$s (see Eq. 4.7) after t_{max}. In Equation 4.7, 75 mm corresponds to the distance between the transducers and the closest end of the specimen. The signal has to travel this distance twice (with a predicted velocity smaller than $v_{g,A0,lim}$) before the first reflection is registered at the transducer. This means that ΔT_Ψ can be considered as a probable 'clean' portion of the waveform following the instant of maximum instantaneous energy content of the signal.

$$\Delta T_\Psi = \frac{2 \cdot 75\,\text{mm}}{v_{g,A0,lim}} = 89.8\,\mu\text{s} \tag{4.7}$$

The first local minimum preceding the end of the interval ΔT_Ψ ($T_{end} = TThr + t_{max} + \Delta T_\Psi$) is taken as the upper bound of the time-integral of the CWT $T_{\Psi 2}$, representing the end of the primary wave packet of interest.

Classification using PCA and GMM Clustering
The intention is to use normalized AE frequency spectra for the classification of damage modes. This leaves the amplitude/energy content of a signal decoupled from the classification problem, allowing it to become a measure of the magnitude of damage rather than the type of damage

Each AE event is associated with two waveforms (one for each sensor), resulting in two, possibly different, (normalized) frequency spectra for each event. For redundancy, the classification algorithm was run on the two datasets of normalized frequency spectra (one from each sensor) independently, which resulted in two classes being assigned to each event. Then, each event was assigned to one of the following classes: high-frequency event, low-frequency event, or undecided. The procedure of event classification is detailed in the following paragraphs.

First, the classification algorithm is run on the two transient AE datasets (one from each transducer) independently: It includes a Principal Component Analysis (PCA) step to identify the principal composition of the normalized frequency spectra and reduce their dimensionality, and a proximity-based event classification using a Gaussian Mixture Model (GMM, see Section 2.3.2) in the space of the first principal coordinate. Finally, events are labeled only if they have been assigned to the same class by the two channels. The remaining events (which have been assigned to different classes based on the frequency spectra measured by the two transducers) are assigned to the category 'undecided'.

Further details on the PCA step: The normalized frequency spectra $\hat{S}_\Psi$ of all waveforms registered at one of the transducers during tensile testing can be stacked into a single dataset, which is then ready to be processed using PCA (see section 2.3.2). Applying PCA will return the orthogonal directions of greatest variance, meaning the most significant, non-redundant contributions to the shapes of the spectra in the dataset, i.e., the principal directions of the dataset.
Figures 4.8 and 4.9 show the mean normalized frequency spectrum (in blue) and the first two principal components of the four datasets of normalized frequency spectra of the waveforms recorded by the two transducers for the two tensile experiments on specimens U7 and U9.
The principal components can be interpreted as features that contribute with different magnitudes to all events in the dataset. Representing the dataset in the space of the first few principal components should automatically capture directions of large variance and separate the points into regions of similarly shaped spectra. This property makes this feature space particularly convenient for an efficient distance-based low-dimensional clustering, such as GMM.

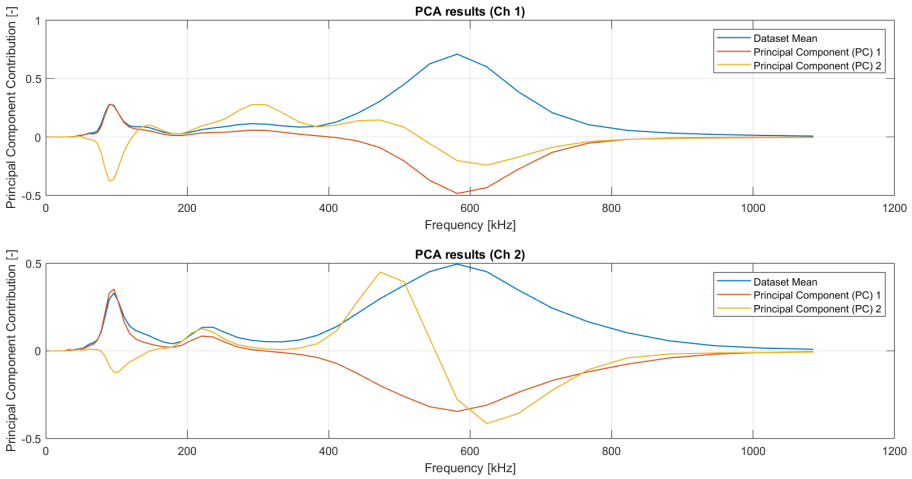

Figure 4.8: Results of PCA: mean and first two principal components of the dataset of normalized frequency spectra recorded by transducers 1 and 2 during testing of specimen U7.

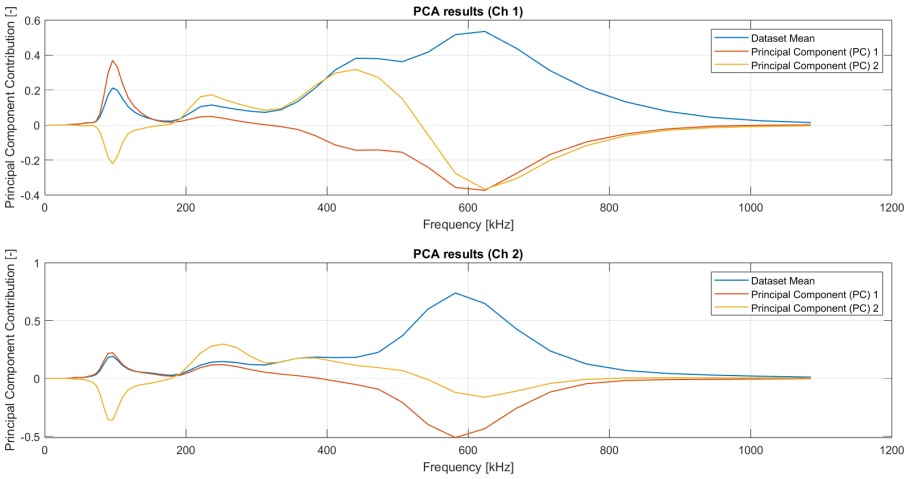

Figure 4.9: Results of PCA: mean and first two principal components of the dataset of normalized frequency spectra recorded by transducers 1 and 2 during testing of specimen U9.

The principal components are unit vectors, and thus the (mean-subtracted) normalized frequency spectra in the dataset can be projected into 2D principal space by performing a dot product with the first two principal components (which is equivalent to a convolution of the signal with the principal component). The two scalar values resulting from the convolution with the first two principal directions can be used as X- and Y-coordinates of each event in 2D principal space. The resulting projections of two out of the four collected datasets into the respective 2D space of principal coordinates are shown in Figure 4.10. The remaining datasets (collected by transducer 1 on specimen U7 and by transducer 2 on specimen U9) can be found in Figure 9.3 in Chapter 9 (appendix).
The scatter plots in Figure 4.10 are colored according to the assigned type of event. The classification was performed using an unsupervised machine learning approach: Gaussian Mixture Models (GMM) with two clusters. The GMM clustering algorithm was run on the (1D) projection of each dataset onto the first principal component, which returned two one-dimensional Gaussian distributions. The Gaussian distributions are characterized by model mean and standard deviation, such that each event has a probability of belonging to either one of the two clusters, depending on its contribution from the first principal component. The event was then assigned to the distribution, which would generate it with the highest probability.

This procedure was repeated twice for each experiment (on specimens U7 and U9), once on each dataset resulting from the two transducers. The result was a twofold classification of each event into a low- and a high-frequency cluster. Whenever the classification using the two transducers agreed for an event, the corresponding class was assigned to the event; otherwise, the event was classified as 'undecided'.

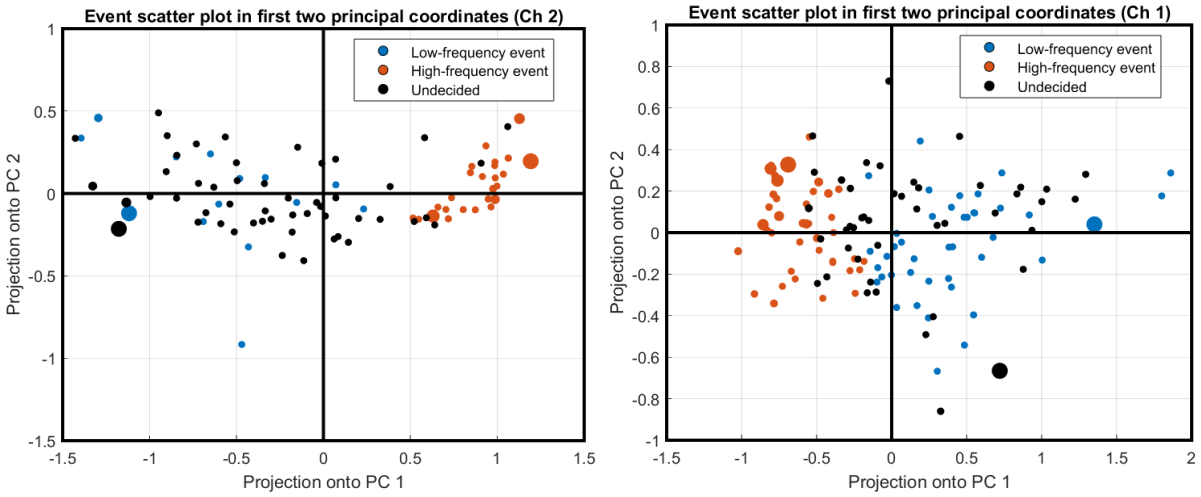

(a) Specimen U7, Channel 2.

(b) Specimen U9, Channel 1.

Figure 4.10: Two out of the four collected datasets projected into the 2D space of principal coordinates.

It has to be mentioned that the classification using one principal component and only two clusters presents a limitation in terms of the specificity of the recognition of damage mode. In this study, it is assumed that the principal components of the normalized frequency spectra are indicative of different damage modes. Looking for more groups of AE corresponding to different areas in the space of principal coordinates (and thus different damage modes) increases the specificity of the event differentiation, but it has also been observed to increase the disparity in classification between the two channels using the current methods. This means that more events were categorized as 'undecided' when increasing the number of clusters. For this reason, the number of types of events has been kept to two in the scope of this work. Increasing that number, however, shall be recommended as future work in the final chapter of this thesis (see Chapter 8).

The novelty of this approach is given by applying PCA to the dataset of normalized frequency spectra directly, without selecting other features in the time or frequency domain in advance. Thus, the shape of the entire frequency spectrum (in the range of $40\,\text{kHz} - 960\,\text{kHz}$) theoretically contributes to the characterization algorithm.

4.4.2. Specimen Inspection using Micro-CT

Micro-CT has been performed at two specified locations per specimen (U7 and U9) before and after tensile loading with a resolution of $8\,\mu\text{m}$. The locations of the two scanned sections are shown in Figure 4.11.

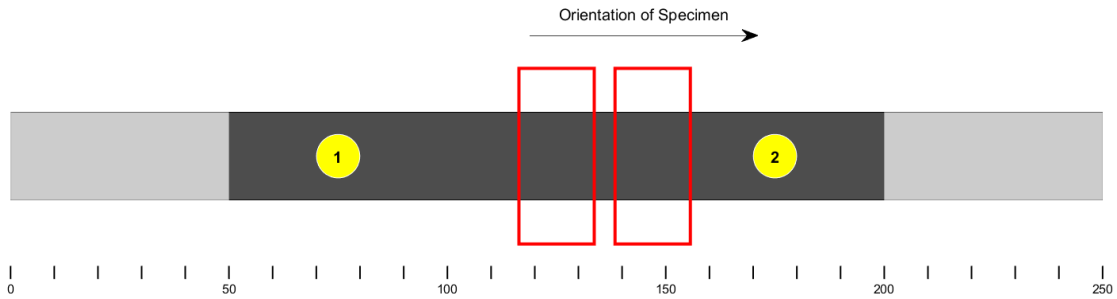

Figure 4.11: Schematic map of the specimen including locations of the AE transducers (yellow circles) and the scanned sections (red rectangles, 'regions of validation').

The scanned sections are called 'regions of validation' in this study, and they are located at the mid-length of the specimen (centered at $x = 125$ mm) and 22 mm to the right centered $x = 147$ mm), and have a width of 17.25 mm.

This results in two (number of scanned locations) times two (number of scanned specimens) times two (before and after tensile testing), which equals eight scans in total. From the set of eight scans, two must be compared at a time (same specimen and location before and after tensile testing). To compare two scans, the tomographic data must be represented in an interpretable format, and for visual comparison, a visually appealing format is preferred. The volumetric data was sliced into 2D frames from the front to the back of the specimen using the image rendering software 'Dragonfly'. This made the size and shape of internal defects and damage most accurately observable. The orientation of the CT images is shown schematically in Figure 4.12.

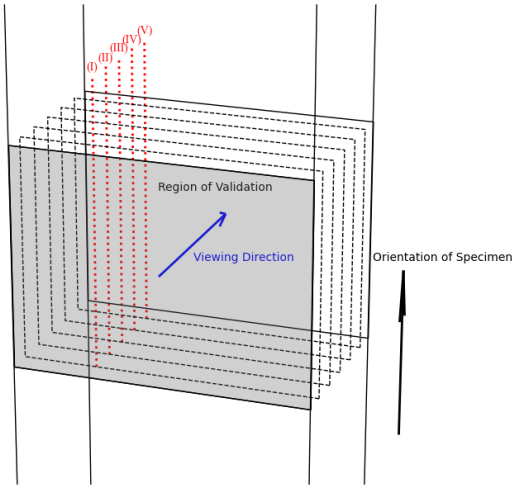

Figure 4.12: Schematic representation of the orientation of CT image frames. The blue arrow indicates the viewing direction of the CT frames. Ply interfaces are pointed at by the red annotation lines.

Figure 4.13: Specimen inside the micro-CT scanner. Scanned regions are marked with strips of tape that indicate the desired alignment of the X-ray cathode.

Basic image processing techniques such as pixel-wise comparison, histogram comparison, and Structural Similarity Index (SSIM) have also been implemented, but the outcomes thereof were rather insufficient. Issues arose due to the scans and the reconstruction of the data being carried out under different conditions before and after tensile testing. The reconstructed tomographic data of the two scans did not overlap properly enough for successful pixel-wise comparison. The implementation of advanced image processing techniques for automated comparison of the tomographic data shall be the subject of further work.

5 Results

The experiment detailed in section 4.3 was run for two specimens (U7 and U9), which included micro-CT scanning and tensile testing to induce mechanical damage while monitoring AEs and locating probable damage hotspots.
The results of the micro-CT scanning of the two specimens before and after the tensile experiment are detailed in the next section, followed by the results of the AE monitoring during tensile testing in Section 5.2 and 5.3.

5.1. Micro-CT Scans

A selection of frames from the preliminary scan (before tensile testing) of the mid-length section (centered at $x = 125\,\text{mm}$) of specimen U9 is shown in Figure 5.1. Defects in the material manifest as dark spots in the scans, which indicate regions of lower matter density, such as voids, air inclusions, and weak interface bonds. The slices are selected in an interval of about 20, which corresponds to the ply thickness of $0.16\,\text{mm}$ ($0.16\,\text{mm} = 20 \cdot 8\,\mu\text{m}$), to capture the imperfections that are expected at the interfaces of the plies.

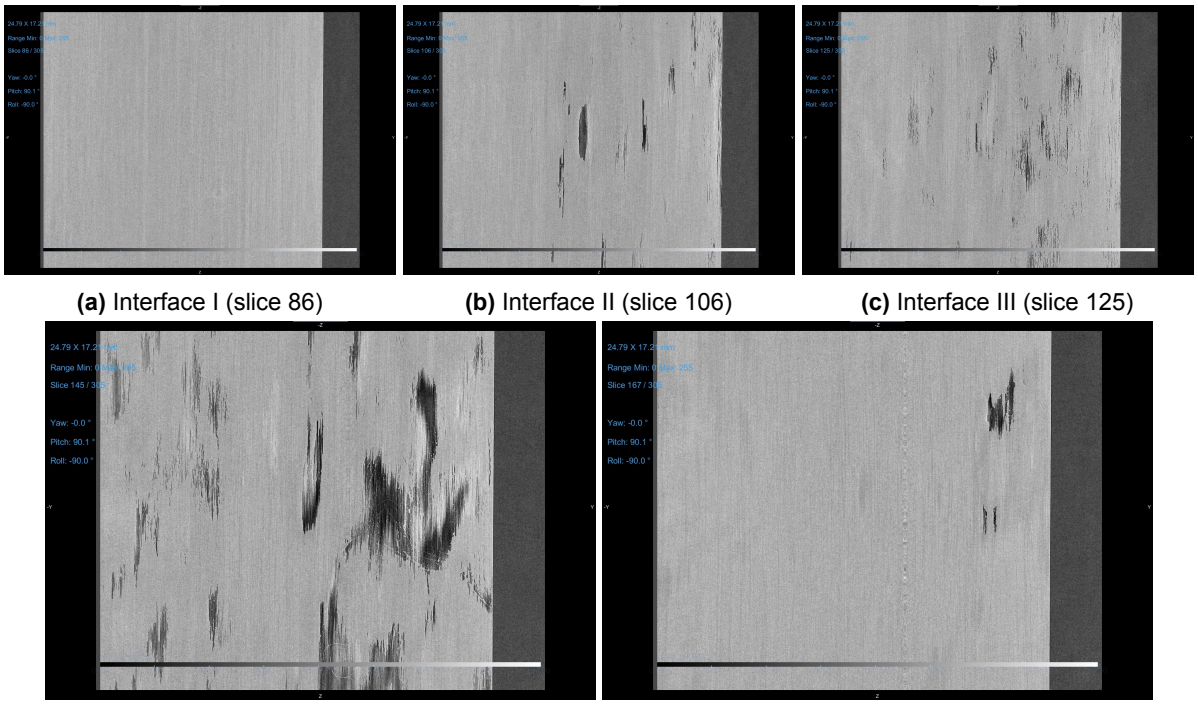

(a) Interface I (slice 86) **(b)** Interface II (slice 106) **(c)** Interface III (slice 125)

(d) Interface IV (slice 145) **(e)** Interface V (slice 167)

Figure 5.1: Preliminary micro-CT of specimen U9 centered at $x = 125\,\text{mm}$ before tensile experiment. Five frames showing the five ply interfaces.

In general, the expected damage modes in the unidirectional specimen under the given loading conditions (i.e., longitudinal tensile loading) are inter-fiber matrix cracks, longitudinal fiber detachment, and fiber fractures. Longitudinal fiber detachment occurs when the epoxy matrix that bonds the fibers cracks along the direction of the fibers due to shear effects that arise at the fiber-matrix interface. This is most likely to happen at the interface between the plies of prepreg, because this is where the bond between adjacent layers of fibers is likely to be weakest due to manufacturing defects in the cured interface. Note that the quality of the bond seems to be best for ply Interface I and worst for ply Interface IV in Figure 5.1.

Please note that a portion of about 3.5 mm is missing from the left of the preliminary scan. This was caused by an issue with the alignment of the specimen with the X-ray cathode that was recognized only after the tensile experiment had taken place. The quality of the scans improved substantially during the second round of scans, which is exhibited in Figure 5.2.

The same selection of frames, but from the scan taken after the tensile experiment, is shown in Figure 5.2. The slice numbering does not correspond directly to the one in Figure 5.1, because scanning conditions varied slightly between the two scans. Nevertheless, the difference in slice numbering corresponds to a physical distance between the slices (measured in units of $8\,\mu$m) and remains consistent across the two scans.

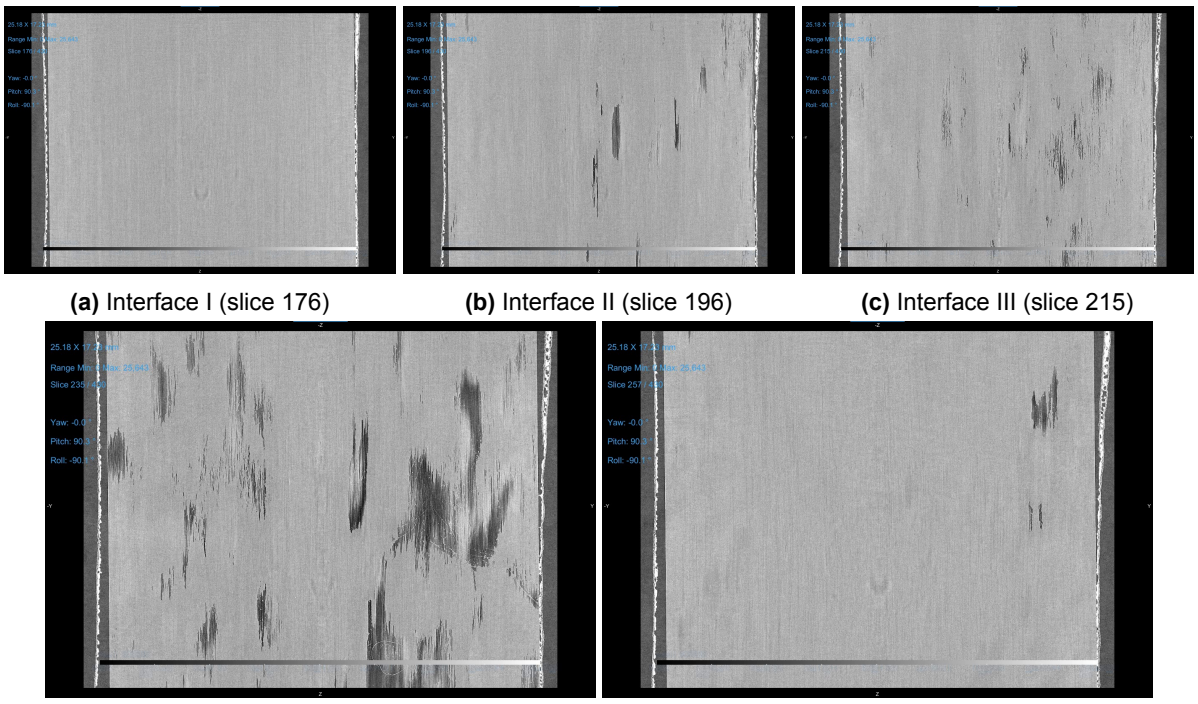

(a) Interface I (slice 176) **(b)** Interface II (slice 196) **(c)** Interface III (slice 215)

(d) Interface IV (slice 235) **(e)** Interface V (slice 257)

Figure 5.2: Follow-up micro-CT of specimen U9 centered at $x = 125$ mm after tensile experiment. Five frames showing the five ply interfaces.

Almost every defect exhibited in the preliminary scan could be associated with an identical entity in the follow-up scan, either in the slice corresponding directly to the one in the preliminary scan or in an adjacent one. Exceptions are structural defects displayed by the follow-up scans that differ in shape and general appearance from the corresponding area in the preliminary scan. Only two exceptions could be found overall by visually comparing the scans of both specimens for all scanned locations before and after tensile testing. They are reported and detailed in the following paragraphs.

The first exception was found in the ply Interface IV of the quarter-length scan ($x = 147$ mm) of specimen U9. The corresponding frames from the scans before and after tensile testing are displayed for comparison in Figures 5.3 and 5.4.

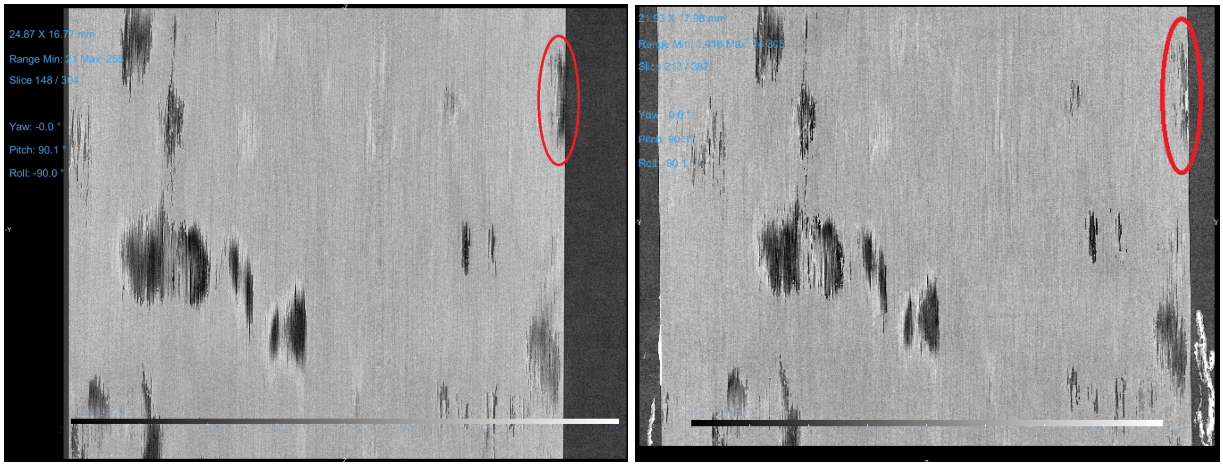

(a) Before tensile testing **(b)** After tensile testing

Figure 5.3: Frames from the micro-CTs of specimen U9 centered at $x = 147\,\text{mm}$ showing the interface IV viewed from the front before and after tensile testing.

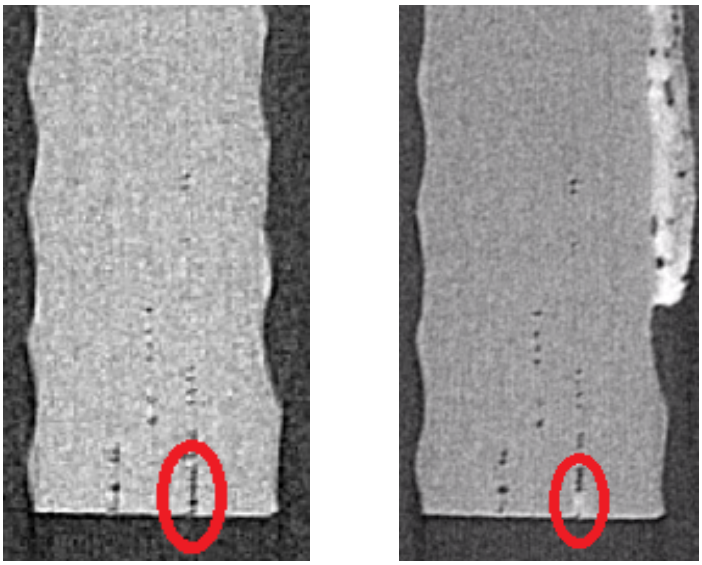

(a) Before tensile testing **(b)** After tensile testing

Figure 5.4: Frames from the micro-CTs of specimen U9 showing a portion of the total cross-section (at $\sim x = 152\,\text{mm}$) viewed from above before and after tensile testing.

The spot circled in red likely corresponds to the location of a damage event that took place during the quasi-static tensile experiment. The damage is located at the right external edge of the ply interface IV and appears as a bright elongated shape (size: $0.22\,\text{mm} \times 0.96\,\text{mm}$) in the follow-up scan that was not present in the preliminary scan. The alteration is consistently present in the follow-up scan over a range of five slices (corresponding to a crack opening of $\sim 0.04\,\text{mm}$), and could therefore not be attributed to an issue in the orientation of the specimen or alignment of the X-ray beam (as was the case for all other major defects in the follow-up scans of specimen U9 that did not appear directly in the corresponding slice of the preliminary scan).

The second exception was found in the ply Interface IV of the quarter-length scan ($x = 147\,\text{mm}$) of specimen U7. The corresponding frames from the scans before and after tensile testing are displayed for comparison in Figures 5.5 and 5.6. The dark area of the defect seemingly shrinks during the tensile experiment (from $0.62\,\text{mm} \times 2.04\,\text{mm}$ to $0.15\,\text{mm} \times 0.24\,\text{mm}$).

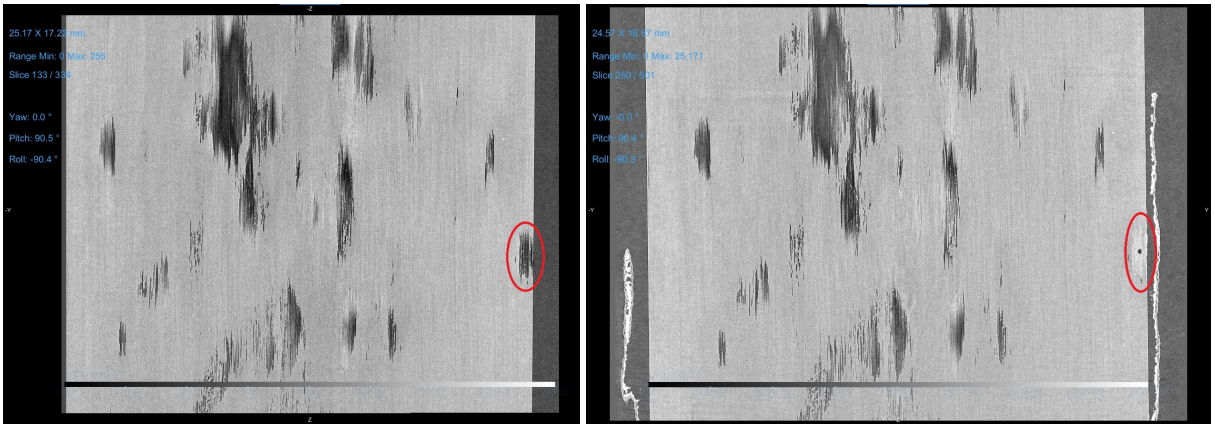

(a) Before tensile testing **(b)** After tensile testing

Figure 5.5: Frames from the micro-CTs of specimen U7 centered at $x = 147$ mm showing the interface IV viewed from the front before and after tensile testing.

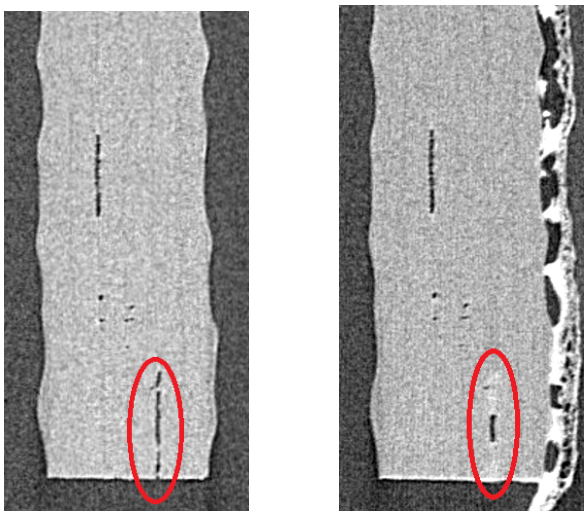

(a) Before tensile testing **(b)** After tensile testing

Figure 5.6: Frames from the micro-CTs of specimen U7 showing a portion of the total cross-section (at $\sim x = 146$ mm) viewed from above before and after tensile testing.

The CT scans of the two locations on the two specimens have been compared frame by frame before and after tensile testing using visual inspection. An attempt was made to automate the comparison using basic image processing techniques such as pixel-wise comparison, histogram matching, and the metric of Structural Similarity Index Measure (SSIM). However, they all failed because the two scans were not perfectly aligned. Automating the comparison while accounting for the small mismatches in specimen orientations and the alignment between preliminary and follow-up scans is a complex task. It requires the use of advanced image processing tools and therefore falls beyond the scope of the current work.

Two hotspots of initiating damage could be identified by visual inspection: one in specimen U7 at location $x = 146$ mm (see Fig. 5.5) and one in specimen U9 at location $x = 152$ mm (see Fig. 5.3). No other visible damage could be identified in the scanned regions using micro-CT with the current setup. In particular, the regions of validation at the mid-length section of both specimens remained seemingly perfectly intact under the applied loads during tensile testing.

5.2. AE Monitoring Framework

During the quasi-static tensile testing in stages of progressively increasing load (by 1 kN) acoustic emissions (AEs) were recorded by the PZT transducers, resulting in 91 events recorded on specimen U7 and 127 events on specimen U9 during the loading phase (i.e. excluding the AEs recorded during clamping and PLB testing).

Figure 5.7 shows the AE events recorded, located, and characterized by the AE monitoring framework detailed in Section 4.4.1 throughout the tensile experiment on specimen U7. The error bars show the plausible localization error that has been measured while validating the TDOA method using PLBs. AEs recorded during clamping (*Time* < 100 s, first the top, then the bottom of the specimen), and the phase of PLB testing (600 s $<$ *Time* < 800 s, at locations $x = 100,\ 125,\ 150$ mm) are also included in the figure.

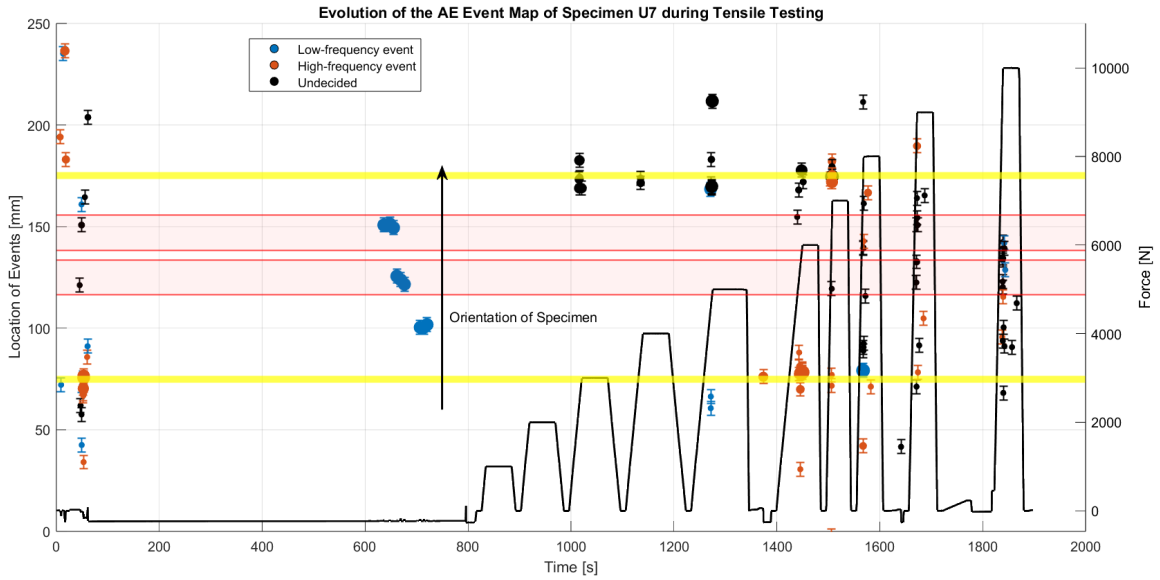

Figure 5.7: Evolution of the AE event map of specimen U7 over the course of the full experiment, showing location, type, and size of AE events over time. The red strips indicate the regions scanned using micro-CT, and the yellow lines the locations of the two sensors.

The Kaiser effect can be observed in Figure 5.7 (with only two exceptions: one at *Time* $= 1374$ s and one at *Time* $= 1635$ s). It refers to the phenomenon observed in materials (particularly composites) under quasi-static loading, where acoustic emissions are only generated when the applied load exceeds the previously experienced maximum load. In other words, no significant acoustic emissions occur until the material is stressed beyond its prior peak load. Deviations from the Kaiser effect (like AEs before the previous maximum load) may indicate an observable reduction in stiffness and in strength due to damage accumulation or fatigue.

Note that during tensile testing, a high-frequency event (Event 51, $E_{\Psi,51} = 0.004\,\text{mV}^2\text{s}$) has been detected in one of the regions of validation (find the waveform in Figure 6.3b). It was located at $x = 145.3$ mm and took place at *Time* $= 1569$ s, during the load of 8 kN. A cascade of further, 'undecided' events was detected in correspondence with this high-frequency event during the peak load of 10 kN at *Time* $= 1840$ s. A high-frequency event (Event 82, $E_{\Psi,82} = 0.003\,\text{mV}^2\text{s}$) was also detected at the bottom boundary of the other region of validation during the peak load of 10 kN (*Time* $= 1840$ s, $x = 118$ mm), but the error in localization makes it probable that this event actually occurred outside of the scanned region. Besides said events, only low-frequency and 'undecided' events occurred in the remaining scanned regions (marked by the red rectangles in Figure 5.7) of the specimen during this experiment.

For specimen U9, it was not possible to retrieve force data due to a malfunctioning of the testing machine's data-acquisition motherboard. Therefore, the force data was artificially recreated using the time stamps of the load levels noted manually in the AE data during the experiment. The evolution of

the damage map throughout the full experiment (including clamping, tensile testing, PLB testing, and unclamping) is shown, with the artificial force data, in Figure 5.8. The loading phase starts at *Time* $= 196$ s and ends after reaching 8 kN at *Time* $= 667$ s. PLB tests happened during $1080\,\text{s} <$ *Time* $< 1147\,\text{s}$.

The clamping into the tensile testing machine of the bottom of specimen U9 had to be repeated twice to increase safety precautions before the mechanical test. The series can be traced back in Figure 5.8: clamping top (~ 20 s), clamping bottom (~ 45 s), unclamping bottom (~ 70 s), re-clamping bottom (~ 155 s). During the re-clamping of the bottom, AEs originated both from the bottom and the top of the specimen. This indicates an effect of strain transfer from one clamp to the other due to the Poisson effect, causing contraction and expansion of the specimen along its length.

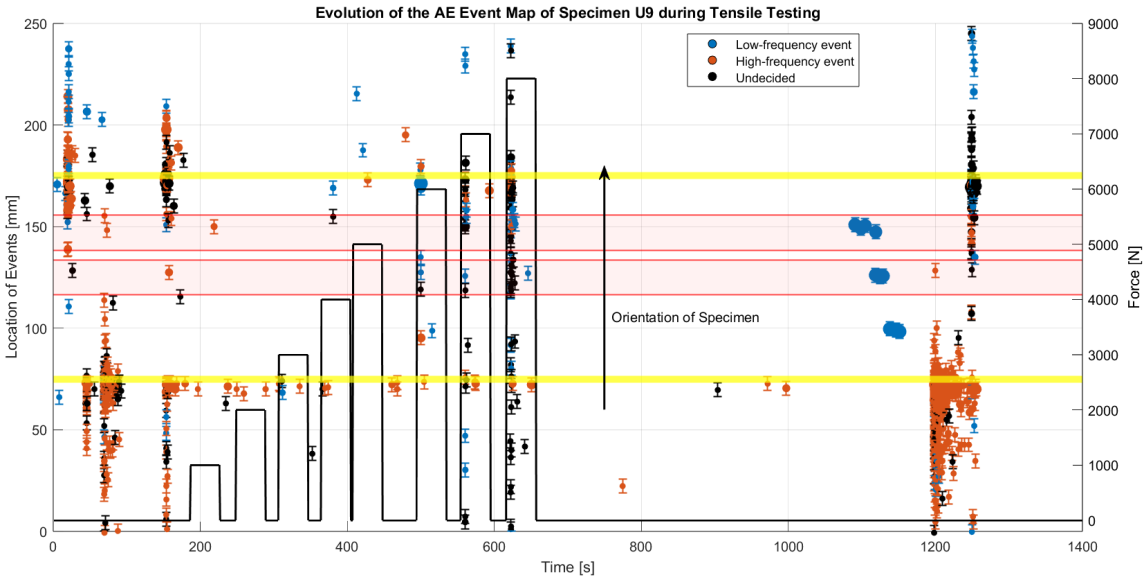

Figure 5.8: Evolution of the AE event map of specimen U9 over the course of the full experiment showing location, type, and size of AE events over time. The red strips indicate the regions scanned using micro-CT and the yellow lines the locations of the two sensors.

Note that during tensile testing a major high-frequency event (Event 2, $E_{\Psi,2} = 0.03\,\text{mV}^2\text{s}$) has been detected at *Time* $= 220$ s in the quarter-length region of validation, located at $x = 151$ mm, during the load of 1 kN (find the waveform in Figure 4.3a). A cascade of major 'undecided' events followed the high-frequency event at this location during the peak load of 8 kN.
Another high-frequency event (Event 96, $E_{\Psi,96} = 0.002\,\text{mV}^2\text{s}$) was recorded at the bottom of the other region of validation ($x = 119$ mm). This event was also accompanied by an entourage of low-frequency and 'undecided' events. However, this second apparent AE hotspot consists of events of smaller size, i.e., with less energetic signals.
A third high-frequency event (Event 119, $E_{\Psi,119} = 0.023\,\text{mV}^2\text{s}$) was found at the top boundary of the mid-length region of validation ($x = 134$ mm). However, the error band of this event reaches outside the region of validation, and, therefore, it is possible that it does not fall within the scanned region at all.

In summary, for specimen U7, only one high-frequency was located into the regions of validation (at $x = 145.3$ mm), in correspondence of the damage shown in Figure 5.5 located at $x = 146$ mm.
For specimen U9, two high-frequency events were located in the regions of validation. The first one at $x = 150$ mm in correspondence with the damage shown by the micro-CT in Figure 5.3, located at $x = 152$ mm. The second high-frequency event was located at $x = 119$ mm and no corresponding visible damage could be identified in the follow-up scan of specimen U9 (shown in Figure 5.2). This could be explained by the fact that the damage is small in size, and since it happens during the last load level (see Figure 5.8), there is no chance for it to grow to a visible size. This explanation is in agreement with the working assumption that the damage size correlates with the energy content of the associated AE event, because the (cumulative) energy content of the first high-frequency event ($x = 150$ mm) and its surrounding 'undecided' events is much larger than the second one (at $x = 119$ mm).

5.3. Categorized AE Frequency Spectra

The frequency contents of all events have been extracted from the recorded AE data, normalized, and categorized according to the methodology in 4.4.1. For each specimen, this resulted in three groups of data ('high-frequency events', 'low-frequency events', and 'undecided'), which contain, for each event, the two normalized frequency spectra of the waveforms recorded by the two transducers/channels.

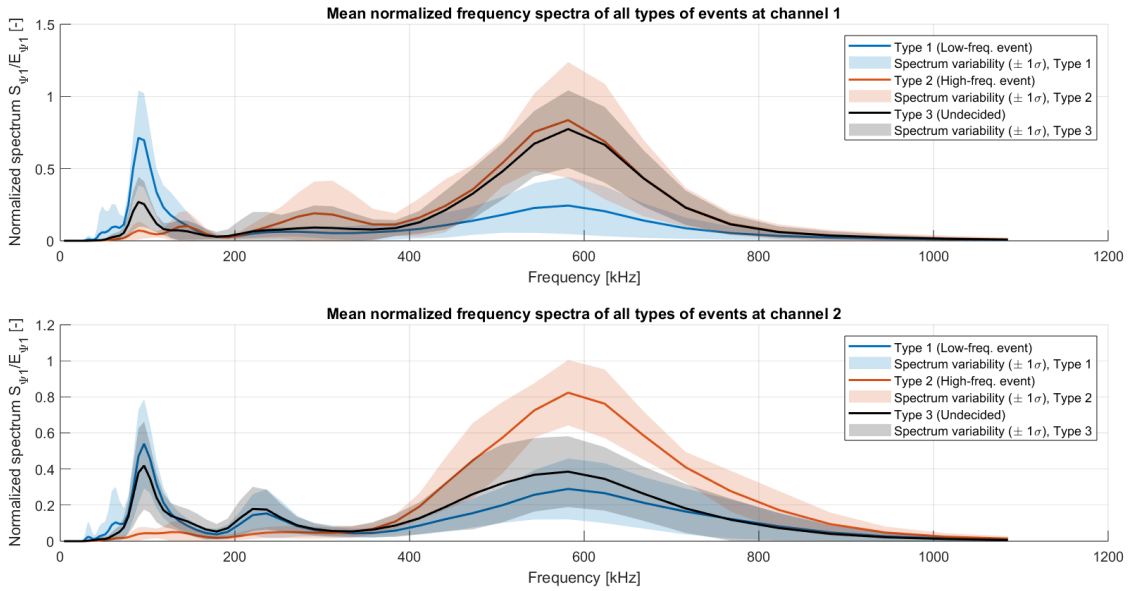

Figure 5.9: Normalized frequency contents of each class/type of events recorded by the two transducers/channels on specimen U7. The datasets of each class are represented by mean value and standard deviation.

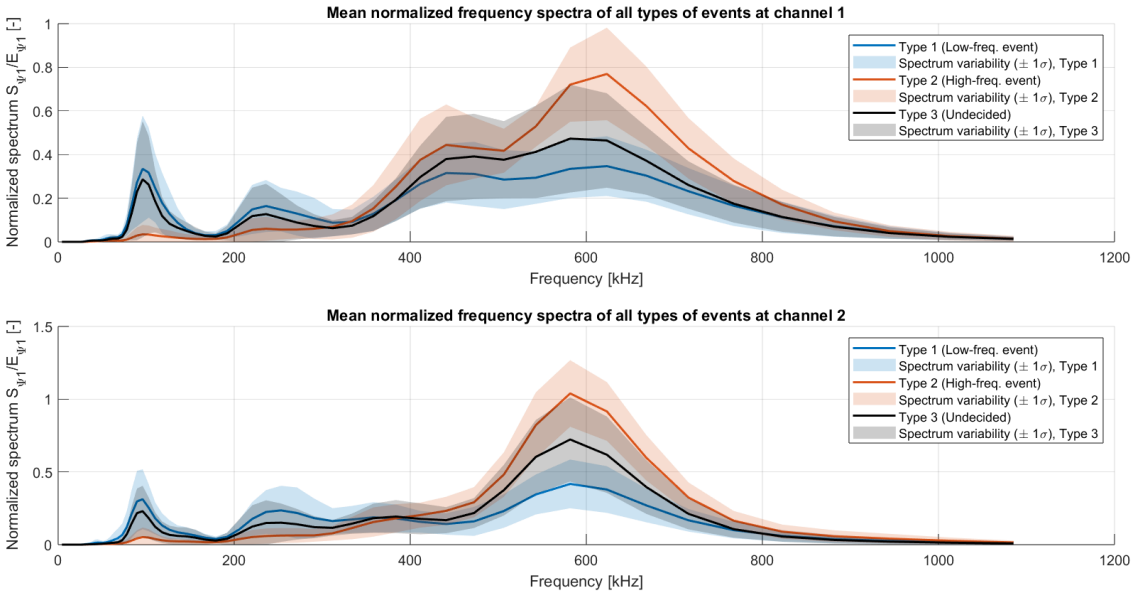

Figure 5.10: Normalized frequency contents of each class/type of events recorded by the two transducers/channels on specimen U9. The datasets of each class are represented by mean value and standard deviation.

Figures 5.9 and 5.10 show the normalized frequency contents obtained using the proposed method (making use of CWT) of each class or 'type' of events, for specimens U7 and U9 respectively. The two datasets (from channel 1 and channel 2) belonging to each class (low-frequency, high-frequency, and undecided) are represented in the figures by their mean normalized frequency spectra and the corresponding standard deviation of all events of that type.
Increasing the number of identified classes to match the number of expected damage modes is desirable, but in the current setup, it has been observed to lead to more inconsistency in the classification of the normalized frequency spectra by the two sensors.

Please note that CWT can create sharper spectra at low frequencies and more blurred (blunt) spectra at high frequencies. This is because narrow wavelets are highly localized in time (good time resolution), meaning they can accurately identify transient events or signals with short durations. However, this comes at the cost of frequency resolution, which explains the broad peak t 580 kHz. Please refer to Section 2.3.1 for further insight on CWT and Heisenberg's Uncertainty Principle.

The AE events are divided into two classes: the blue and red classes (low- and high-frequency events). The two classes are characterized by signature energy peaks at two different frequencies: at ~ 100 kHz for the low-frequency type of events, and at ~ 580 kHz for the high-frequency type. Note that the high-frequency class of events recorded on channel 1 in specimen U7 shows a secondary peak at ~ 300 kHz and a large standard variance compared to the other high-frequency datasets. The classes of low-frequency and undecided events have a secondary peak at ~ 230 kHz in all datasets, except the one generated by transducer 1 on specimen U7 (Fig. 5.9, top). The frequency spectra from sensor 1 on specimen U9 (Fig. 5.10, top) show larger contributions in the range of $400 - 500$ kHz than the others do.
Another notable observation is that the low-frequency datasets of specimen U9 (Fig. 5.10) have flatter shapes with the peak at ~ 100 kHz less pronounced and stronger high-frequency contributions than for specimen U7. The flatter shapes of the low-frequency datasets from specimen U9 in Figure 5.10 than for specimen U7 in Figure 5.9 may be caused by differing sounds of damage, or be an indication of different monitoring conditions between the two tests. Differing damage sounds may be caused by different damage mechanisms dominating in the two experiments, or by the different clamping conditions causing different boundary interactions of the elastic waves at the ends of the specimen (remember, a fixed mechanical clamp was used for testing specimen U7, while specimen U9 was clamped using automatically adjusting hydraulic grips). Different monitoring conditions are unlikely because all setup parameters from the test on specimen U7 were reproduced for the second test on specimen U9. However, even small differences in the monitoring setup can lead to different signal transfer functions, causing e.g. a right-shift of all spectra as is seen in Figure 5.10 compared to 5.9.

The class of 'undecided' events contains all the events that were classified inconsistently using the normalized frequency spectra generated by the two transducers. For specimen U7, the mean frequency spectrum of this class at transducer 1 looks similar to the high-frequency mean, but at transducer 2, it is more similar to that of low-frequency events. This sheds doubt on the consistency of the frequency spectra of different damage modes, at least when extracting them with the current method. More on this subject in Section 6.3 of the following chapter.

To summarize the findings from the AE data the author would like to stress that two principal types of signals were distinguished in the scope of this work: One type with a peak frequency contribution of 95 kHz and one with a peak frequency contribution of 580 kHz.
The high-frequency type with a peak at 580 kHz seems to indicate locations that are in agreement with the damage visible in the micro-CT scans.

6

Discussion

6.1. Micro-CT Scans

The Micro-CT scans were performed to assess the internal state of the material non-destructively before and after the specimens were subjected to tensile loading. The objective was to compare the scans to identify the mechanical damage generated during the loading experiment. The suspicion was that many defects would already be present in the material before loading due to the manual prepreg layup process. This type of manufacturing increases the risk of imperfect adhesion of successive plies of prepreg. For this reason, the five slices in Figure 5.1 (and Fig. 9.1) showing the state of the interfaces between two successive plies have been chosen, and indeed, the preliminary scans already show imperfections and voids in the specimens before they have been subjected to any loading. This means that they probably stem from manufacturing. The defects were likely caused by the use of expired prepreg material and the vacuum system's failure to ensure proper adhesion of the plies prior to oven-curing, likely due to material embrittlement. The dark spots in Figure 5.1 probably correspond to voids, air inclusions, and generally weak ply bonds.
These defects in the 'pristine' specimens affect the type of damage to be expected during tensile loading. The unidirectional specimens for tensile loading had been designed with the intention to induce and isolate the sound of fiber fractures, but the type of defects shown by the preliminary CT scan probably favored the development of other types of damage in the composite material (like longitudinal fiber detachment and delaminations) as well. Nevertheless, during a major damage event in a unidirectional fiber-reinforced composite, i.e. a permanent deformation visible in a micro-CT image, fiber fractures are expected to occur: If fibers remain perfectly intact, it is unlikely that a visible difference will appear in the micro-CT scans of the unidirectional specimens that consist of more than 50% of carbon fibers ($V_f = 54.4$%). Therefore, visible changes in the internal meso-structure of the material are thought to be caused by a combination of fiber fractures and fiber-matrix debonding/longitudinal matrix cracks.

A few remarks on the comparison of preliminary and follow-up scans (e.g. Figures 5.1 and 5.2):
Note that the micro-CT images before and after the quasi-static tensile experiment are comparable using visual inspection. Small defects in the 'pristine' specimen, up to a few pixels in size (in the range of $20\,\mu$m with the given resolution of $8\,\mu$m), could be identified in the preliminary scans (Figure 5.1) and recognized at the same locations in the corresponding follow-up scan after the tensile experiment had taken place (Figure 5.2).
Sometimes, defects did not appear in the same plane but in one of the adjacent slices. This happens because it is almost impossible to reproduce the scanning conditions exactly in terms of orientation and alignment up to a few micrometers. Nevertheless, almost all internal structural features and defects visible in the follow-up scans could be associated with an identical entity in the preliminary scan.

The only two exceptions were found at $x = 146$ mm in specimen U7 and at $x = 152$ mm in specimen U9. They are reported in Figures 5.3-5.6. In both cases, the dark area seemingly becomes smaller, and bright artifacts are introduced in the follow-up scans after the tensile experiment compared to the preliminary scans. A bright elongated entity appears in the follow-up scan in Figure 5.3b, and the area directly surrounding the highlighted defect in Figure 5.5b also appears brighter than the rest of the material.

Why might a damaged area appear brighter than its surroundings and than the same area in the preliminary scan? One possible explanation is an effect of densification or compression of the material

caused by the microstructural rearrangement during the damage event. Such densified areas absorb more photons, making them appear brighter in CT images. This could have happened in specimen U9, for example, if a residual out-of-plane stress caused by the adhesive force at the ply interface in the 'pristine' specimen was pulling fibers from one ply to the other. This would cause them to warp slightly in the out-of-plane direction and contribute to the adhesive force between the two plies in that region. This pretensioned state, coupled with a low-quality adhesion in this region (which is recognizable already before tensile testing in Figure 5.3a), may have been released during tensile loading, as the two plies detached in this region and slid slightly relative to each other. This would probably cause fiber fractures and the initiation of an edge delamination. As the pretensioned state is released, the fibers that were being pulled out of shape may break and return to their natural and denser packing state, which may explain the bright entity in the follow-up scan. Isolated fiber segments may appear denser than fibers integrated in the matrix because of the lack of residual tension from the surrounding material.
Another possible explanation is that the brightness increases in this area due to the effect of crack interfaces and phase contrast. As the edge delamination initiated in specimen U9, space was created between the two plies, and two new interfaces with air appeared. Interfaces can generate absorption and refraction artifacts, artificially enhancing brightness at edges due to refracted photons, causing a peak in brightness in high-resolution micro-CT. For example, the place where two plies separate with a specific distance may appear bright due to the photons getting trapped by reciprocal reflection at the two interfaces. Another effect of phase contrast could be that, after the two plies separate during the damage event, the area where they touch may appear brighter than the surrounding void that has been created.
The explanations for the bright shape in the follow-up scan can be manifold. Nevertheless, an alteration in the internal structure can be observed that is subtle and localized, not widespread, indicative of initial-stage damage during tensile loading. The observed damage probably consists of a combination of fiber breakages and an initiating edge delamination.
This type of damage would be expected to grow in the horizontal direction, towards the left, if subjected to a mode III type of loading.

The defect of specimen U7 highlighted in Figure 5.5b has bright surroundings, while the corresponding area in the preliminary scan is rather dark. A possible explanation is that the defect in the preliminary scan (Fig. 5.5a) shows a weak or faulty bond between the plies that results in the formation of the damage hotspot that is visible in the follow-up scan (Fig. 5.5b). Again, it may be that residual stresses in the 'pristine' specimen are released by the damage event during tensile testing, causing the previously strained region to recompact as it is relieved of its residual stresses. This may explain the brighter shading around the presumed damage hotspot in Figure 5.5b. The observed damage probably consists of a combination of fiber breakages and debonds/longitudinal matrix cracks.
This type of damage would be expected to grow in the vertical (i.e. longitudinal) direction, if subjected to a mode II type of loading.

The findings derived from the micro-CT scans are summarized in Table 6.1.

Specimen	Horizontal location x [mm]	Proposed damage type	Crack-driving mode
U7	146	Fiber debond/longitudinal matrix crack	II
U9	152	Initiating edge delamination	III

Table 6.1: Characteristics of the two damage hotspots from Figures 5.3 and 5.5.

So, in conclusion, major visible damage due to tensile loading of the specimens was observed to initiate at the imperfect interfaces of the prepreg plies, and in association with fiber fractures, followed by other forms of damage (fiber debonding and ply delamination).

6.2. AE Monitoring Framework

The acoustic emissions (AEs) recorded during tensile testing of the two specimens are visualized in Figures 6.1 (U7) and 6.2 (U9).

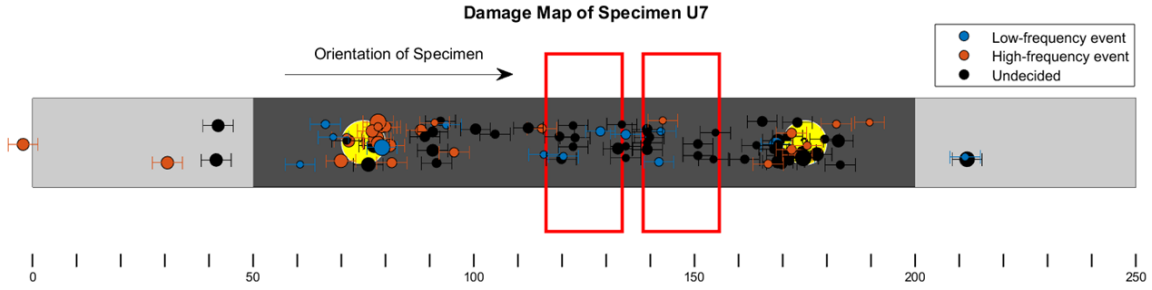

Figure 6.1: Damage map of specimen U7 (maximum load: 10 kN), showing events registered during tensile testing only. (Note that the vertical coordinate of the event locations is a random variable introduced for better visualization - events are located only along the length.)

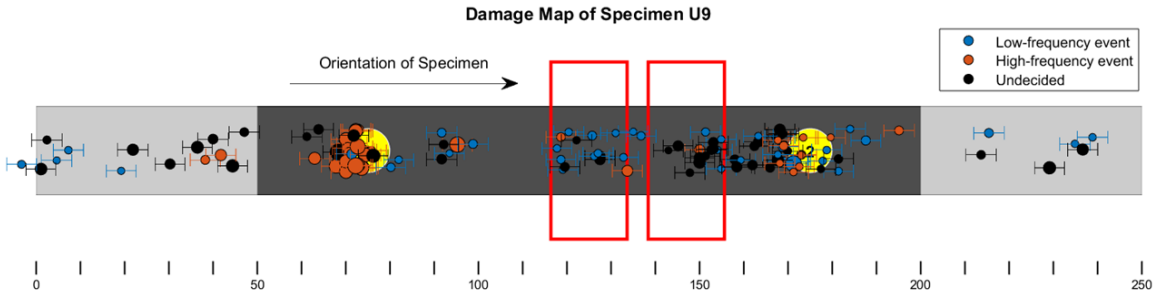

Figure 6.2: Damage map of specimen U9 (maximum load: 8 kN), showing events registered during tensile testing only. (Note that the vertical coordinate of the event locations is a random variable introduced for better visualization - events are located only along the length.)

In general, it must be noted that many more AE events have been recorded than visible damage has been identified in the micro-CT images (compare Table 6.1 and Figures 6.1 and 6.2). At least so is the case for low-frequency and undecided AE events.

The locations of high-frequency events, however, are in agreement with the damage hotspots visible in the scans.

Furthermore, the number of events classified as 'undecided' was relatively high for both experiments, meaning that many events were assigned to a different category when using the waveforms recorded by the transducers at the two ends of the specimen.
This was the first hint to shed doubt on the conventionally defined notion of high-frequency AEs corresponding to fiber fracture events and low-frequency events to matrix damage. A novel interpretation will be proposed in the next section that may, if true, resolve this common inconsistency.

6.3. Categorized AE Frequency Spectra and Waveforms

In the previous chapter and also in the previous section, it has been hinted at that there was often an inconsistency in the frequency spectra extracted from the two waveforms registered by the two sensors. This does not necessarily imply that damage events do not generate consistent signals at their source, but it does shed doubt on the consistency of frequency spectra extracted from the waveforms registered at the transducers with the current methodology.
This common inconsistency led to many events being classified as 'undecided', and to the question as to

why the frequency contents of the events often appeared so different at the two transducers. This question will be given a possible answer in the following paragraphs.

There are a few steps of transmission and signal processing between the sources of the AEs and the generated frequency spectra. Every transmission step (through the specimen, between the specimen and the transducer, and between the transducer and the digital signal) has its respective complex transfer function in the frequency domain. So, even if damage modes do emit AE signals with consistent frequency contents at the source, they may still appear differently at the end of the chain of transmission. There is the suspicion that dispersion (and visco-elastic damping) of the mechanical wave along the length of the specimen may distort the frequency contents of the waveforms at the two transducers. In particular, this effect probably delays the detection of low-frequency contents at the sensor further away from the source. Combined with the frequency-content-extraction method from Section 4.4.1, which limits the window of analysis of the waveform using minima of the instantaneous energy content (see Figures 4.6), this may lead to low-frequency contributions being effectively omitted from the spectra of some waveforms. This effect can be observed in Figure 4.7, where the spectra from the sensor further away from the source (Ch 1) seem generally skewed to the right, toward higher frequencies, compared to the spectra from the sensor closer to the source (Ch 2), because low-frequency contributions arrive late due to dispersion and are partly cut away with the back of the waveform.
Please refer to the final chapter on recommendations for further work for a suggestion on how to improve the current method to counter the effect of the distorted frequency contents due to the length of the path of propagation.

Observing the effect of dispersion, causing many events to be classified as undecided, led to a key insight about the recorded waveforms that will be exposed in the upcoming paragraph.
In general, most of the recorded waveforms have been observed to consist of a high-frequency head, followed or not by a lower-frequency tail (see Figure 6.3), which was the key feature distinguishing low- from high-frequency events.

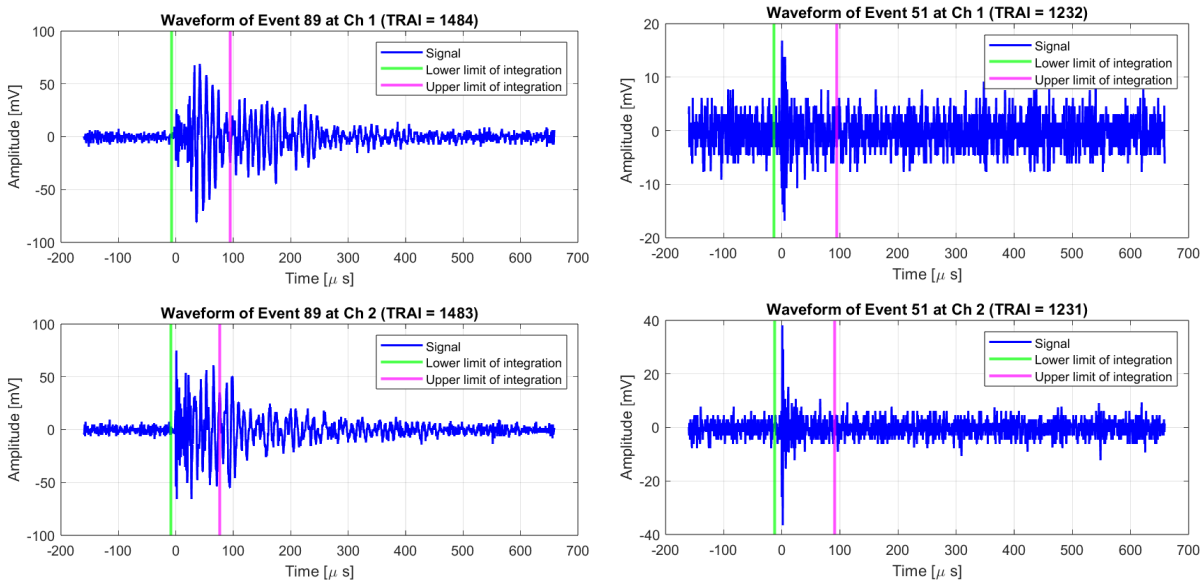

(a) Sample low-frequency event ($x = 128.7$ mm). **(b)** Sample high-frequency event ($x = 142.8$ mm).

Figure 6.3: Waveforms of two sample events from specimen U7.

In undecided events, the low-frequency tail may be included by one channel, but not by the other, leading to inconsistent classification. See e.g., in Figure 4.3b, the waveform of Event 18 from specimen U9 ('undecided'): The sub-period of integration includes almost the whole wave packet for the sensor closest to the source (Ch 2), but, due to dispersion, only the high-frequency wave packet is fully included in the

waveform registered by the sensor further away (Ch 1). In Figure 4.5, this effect can be observed in the CWT of that same event as well.

This observation concerning the recorded waveforms of 'undecided' and low-frequency events led the author of this work to stipulate the interpretation laid out in the following paragraph.
The common understanding in the literature is that low-frequency events are associated with matrix damage and high-frequency events with fiber fractures. However, there is a possible alternative interpretation: A low-frequency tail may be observed in the emanated waveform when a fiber fracture occurs, but the surrounding material remains intact, and some of the released strain energy remains conserved in the form of a lower-frequency elastic vibration, effectively halting the further ripping of the surrounding material. High-frequency events, on the other hand, do not have such a tail, which might suggest that the fiber fracture leads to further ripping of the matrix, instead of being halted by it. In this narrative, during a high-frequency event, strain energy is consumed by further ripping of the material, which leads to the creation of a (contagious) damage hotspot. Hence, the absence of a low-frequency tail may be an indication that the event included a large and visible surface detachment internal to the material. This would explain why low-frequency events are located all over the material and high-frequency events only in correspondence with damage visible in the micro-CT.
If this explanation is true, this would mean that, contrary to common belief (and to an assumption made at the beginning of this work), the energy content of the elastic wave is **not** an indication of the size of damage. It is rather the absence of a low-frequency tail that indicates a visible rip in the material.

Whichever the explanation, the result holds that in the current setup, the locations of (early) high-frequency events (with a peak at 580 kHz) are in agreement with the locations of damage observable in the micro-CT scans. Moreover, many low-frequency (100 kHz) events have been located in regions where no damage could be identified in the micro-CT. This may indicate that early high-frequency events announce the development of visible damage in later stages, when the load is increased. Visible damage has been associated with fiber fractures, because that is the damage mode expected in association with 'large' (order of ~ 0.1 mm), plastic, structural changes in the unidirectional composite that are visible in the micro-CT with the naked eye. This may lead to a similar conclusion as Kempf et al. [21], who state that the AEs of fiber fractures have a peak contribution in the frequency range of $450 - 800$ kHz.
However, no further statement can be made, with the current information, about the differentiation of AEs of inter-fiber or transverse matrix cracking, fiber-matrix interface failure, and delamination. That information may be contained in the 'undecided' events that were located in correspondence with the two damage hotspots on specimens U7 and U9, but requires further analysis.

7

Conclusions

In this final chapter, the main conclusions of the research are presented. These findings are discussed in relation to the research questions and initial objectives, highlighting the contributions made and the limitations encountered.

Research Questions **(I.a-c)** refer to the AE monitoring and analysis framework worked out in the context of this thesis. They tackle the topic of damage characterization using frequency and energy contents independently of each other.

The first question **(I.a)** tackled the issue of identifying the length of the measured signals that is representative of the elastic wave packet and not tainted by noise, reflections, or lingering sensor response. The method was based on a transient frequency analysis using CWT, and the key point was the choice of the sub-interval of the waveform from which to extract 'clean' frequency information. This sub-interval is also referred to as 'clean primary wave packet' in Chapter 4. The extraction of a clean primary wave packet, excluding frequency contents of noise and boundary reflections, is tentatively considered successful for the scope of this work, but requires further analysis. Specifically, one of the observed issues was that the identified clean primary wave packet contained different frequency contributions for the two sensors. This often led to events being classified as undecided, simply because dispersion had caused the frequency contents to separate and low-frequency contents to get lost in the waveform behind the upper limit of integration at the sensor furthest away from the source. This happened e.g. for Event 38 of specimen U9 that is shown as undecided in Figure 4.7, because the low frequency content was included in the waveform from sensor 2, but got lost behind the limit of integration at sensor 1 (see Figure 4.3 showing the respective waveforms). This is a limitation of the current setup, but it also became a chance to exploit the information of the head and the tail of the waveforms separately.

The original objective of this work, as expressed by RQ **(I.b)**, was to devise a classification scheme that would take into account spectrum shape in a more granular way, including narrow peaks or common combinations of peaks instead of energy content over a range of frequencies. The PCA applied to the generated datasets should, in theory, have been able to highlight such structures and allow to achieve a detailed insight, but it was limited by the quality of the normalized frequency spectra that were delivered to it by using CWT. The method seems to have been successful in differentiating groups of high- and low-frequency spectra qualitatively, but, at the same time, it lacks the narrow-peak sensitivity necessary to differentiate spectra of different types within the super-categories of high- and low-frequency events. This issue is probably caused by the generation of frequency spectra using CWT, which leads to a lower frequency resolution of the spectra for high frequencies due to Heisenberg's Uncertainty Principle as detailed in Sections 2.3.1 and 5.3. The generation of frequency spectra using an improved signal processing method shall be the content of further recommended work. CWT seems promising in terms of identifying the duration of the wave packet, but it is limited in terms of extracting precise frequency information.

The second part of RQ **(I.b)** covers the question whether different damage modes really do emit elastic waves with characteristic and universally recognizable frequency contents, and it could not yet be answered with confidence.

Finally, research sub-question **(I.c)** tackled the concrete association of families of AE frequency spectra with expected damage modes in the composite material that are visible in the micro-CT scan. Some uncertainty from RQ **(I.b)** was carried on into this problem, so it was not possible to definitively associate an AE frequency spectrum with a corresponding damage mode yet. However, a possibly novel insight was

gained that is exposed in Section 6.3. In summary, it states that low-frequency tails may be indicative of fiber fractures that were 'caught' by the surrounding material, whereas high-frequency events are produced when fiber fractures lead to a further permanent structural change in the surrounding material.
This, if true, may be one of the major findings of this work in terms of characterization of acoustic emissions of damage modes in composite materials under tensile loading: Contrary to common belief, low frequency AE events may not indicate matrix cracking in this context, but instead, they may indicate fiber fractures that are caught by an intact matrix surrounding the fractured fiber, which prevents the fracture from spreading into the surrounding material.

Research Question **(II)** tackled the feasibility of using micro-CT as a validation method that can visualize micro-structural damage in composite materials. Micro-CT was established to be a powerful and useful method to identify damage at the meso-scale, i.e., the dimension of a ply of prepreg, 0.1 mm. The first sub-question **(II.a)** was answered partially successfully. The first finding was that the images taken before and after tensile loading were indeed visually comparable with the naked eye. All visible shapes and entities up to a few pixels in size were found to match between the two scans, which corresponds to a defect size in the order of ~ 0.05 mm $= 50\,\mu$m. However, in practice, the smallest difference that could be spotted using visual inspection of the images was in the order of $\sim 200\,\mu$m. Comparison using basic automated image processing techniques failed because it would have required a perfect alignment of two tomographic datasets, which was impossible to achieve with a manual pre-processing step. The implementation of advanced image comparison tools, possibly using machine learning and convolutional neural networks (CNNs), may be the subject of further work to automate and improve the comparison of the scans. In conclusion, based on the scans, it was possible to make an educated assumption as to the kind of damage that took place, but the images are open to interpretation to some extent. In particular, the reason as to why an increased brightness can be observed in the damaged regions remains in question, although a few possible explanations for this phenomenon are given in Section 6.1.
To answer sub-question **(II.b)**, the highest attainable resolution using the current specimen (with a width of 20 mm) was $8\,\mu$m. It turns out that this resolution is high enough to observe many defects at the interfaces of the plies (that are 0.16 mm thick) and to identify the orientation of the fibers in each ply with the naked eye. However, true micro-damage, such as single fiber fractures, is simply too small still to be found using visual inspection only (in the order of ~ 0.01 mm). As previously mentioned, the smallest damage that was identified has a width of 0.15 mm, and damage up to a size of 0.1 mm could likely still be found by visual inspection, but beyond that it starts to get very challenging with the current resolution. This work suggests that the smallest damage events that generate detectable acoustic emissions may lie in a range that is undetectable by micro-CT in the current setup, i.e., in a size-range $< 100\,\mu$m. Refer to Section 8.1.2 in the next chapter on recommendations for future work to learn that increasing the resolution is an option, but it stands in question whether it will lead to further insight.

To summarize the major contributions of the current work the author would like to point out that acoustic emission monitoring has been confirmed yet again as a powerful and insightful tool to monitor different types of mechanical events on the surface and/or the inside of composite materials (see Figures 5.7 and 5.8). Moreover, the combination of AE monitoring and micro-CT scanning has been proven to be a powerful (if yet in some ways limited) way to confirm and/or put into question the common understanding of damage-induced AEs in composite materials. A novel conclusion that is proposed in this work is that many low-frequency events may not be caused by matrix damage at all, but instead be the result of fiber fractures that are caught by an intact matrix surrounding the fractured fiber.

8

Outlook and Further Work

The final chapter of this thesis covers further recommended work and an outlook on a possible application of the developed (and improved) monitoring system. Recommendations for further work aim at improving the current state of the experimental approach to deliver even higher-quality results and offer further insight into the acoustic emissions of micro-damage in composite materials. The second section will offer an outlook on a possible application of the AE monitoring framework for research purposes in the field of mechanical fatigue degradation of composite materials

8.1. Recommendations for Further Work

In the first section of this final chapter, a few points for improvement of the current experimental framework will be laid out.

8.1.1. Analysis of AE Data

First, direct your attention towards the problem of dispersion and visco-elastic dissipation of the signals as they travel along the length of the specimens to reach the transducers. It was observed that, with the current method of generating frequency spectra, the frequency content is affected by the distance traveled by the signal, because part of the waveform at the end of the wave packet may be cut off. The redundancy of the measurements caused by using two transducers led to the discovery of this problem. In future work, attempts should be made to reduce the impact of the signal transfer function of transmission along the length of the specimen by taking into account the location of the source and the distance traveled by the signal.

A simple way to do this is to do this is to limit the analysis to waveforms registered by the sensor closest to or furthest away from the source of the AE. Two sensors are still necessary to locate the source longitudinally, but only one waveform shall be used. Using the waveform of the sensor closest to the source will probably result in higher fidelity to the original waveform at the source of the signal. Using the waveform of the sensor furthest from the source, on the other hand, may provide an advantage in dissecting frequency contents, because they separate along the path of transmission due to dispersion.

A rather more complex way to compensate for signal transmission along the length of the specimen is the reconstruction of the signal at the source using the sensor transfer function, material dispersion curves, and, possibly, dissipative properties of the material in a time-reversal method. Attempting to reconstruct the signal at the source is challenging, but it may result in an increased consistency of the recorded data (if damage modes are proven to emit consistent waveforms at the source of the sound).

Focus still on the method used to generate the (normalized) frequency spectra from the registered waveforms: It starts with the identification of a 'clean primary wave packet' using local minima of the (smoothed) instantaneous energy content (see Figure 4.6). Frequency spectra are then generated by integrating the CWT over the identified length of the clean primary wave packet.

The advantage of using CWT to generate frequency spectra by integration is that the resulting resolution of the frequency spectra is consistent for all waveforms of all lengths. Other methods (e.g., DTFT) may cause problems of inconsistency of resolution when using waveforms of different lengths, but they may also lead to higher quality frequency spectra, so they are worth looking into. Applying PCA to higher-quality frequency spectra may lead to the identification of more characteristic peaks and combinations of peaks corresponding to specific damage modes. Higher precision in the classification of the frequency spectra

might make it possible to increase the number of clusters beyond two to represent the real number of different expected damage modes.

8.1.2. Micro-CT Image Processing

The comparison of two micro-CT datasets is a complex task that can benefit greatly from automation using advanced image processing tools based on machine learning and convolutional neural networks. It is worthwhile to undertake this challenge if high-quality tomographic datasets are available, which contain information about the presence of damage, at least potentially, waiting to be extracted.
High-quality tomographic datasets are tomographic images, in which the specimen was properly aligned with the cathode tube, and the full width is captured by the scan. This was the case for the follow-up scans after tensile testing (which were of high quality) but not for the preliminary scans, in which about $3.5\,$mm is missing from the width on the left side of the specimen.
Another aspect to consider is the resolution. In theory, the resolution can be doubled compared to the current value, up to $4\,\mu$m. For this to be possible, the specimens' width must be reduced to half the current width. It is possible, in theory, that single fiber fractures ($d_f = 7\,\mu$m) may become visible with such a high resolution. Nonetheless, it stands in question whether this would be desirable at all. Doubling the resolution would also mean doubling the required precision of alignment, which has already been proven to be challenging. Moreover, it is unclear whether a resolution of $4\,\mu$m will make more micro-damage visible in addition to the meso-scale damage visible in the $8\,\mu$m-resolution CT scans of this work. It is possible that micro-damage, such as single fiber fractures without surrounding material ripping, remains invisible with a resolution of $4\,\mu$m, because the crack opening length (without applied tensile tension) might be much smaller yet. In that case, the meso-scale damage will still be the only one visible, making the increased effort unjustified.

8.2. Mechanical Characterization and Fatigue Testing Campaign

The proposed mechanical characterization campaign is intended as an outlook and represents a possible application of the AE-based damage mode monitoring framework for studying fatigue in fiber-reinforced composites. The aim is to continuously predict the remaining fatigue life throughout the specimen's lifetime. This second experimental campaign would involve a static characterization and tensile fatigue testing of similar unidirectional carbon fiber coupon specimens to those in Section 4.1 while monitoring acoustic emissions.

8.2.1. Static Characterization

The phase of static testing of progressively increasing load serves to characterize the material's mechanical behavior both in pristine and in a damaged state.
It is proposed to increase the tensile load in stages, then relieve the specimen completely and subsequently increase the load once more from zero to the next level where AE activity starts once more. States in which no AE activity is recorded shall be known as 'stabilized damage states'. In such a state, the fatigue life of fibers may be determined by their micro-plastic energy dissipation during plastic loading. The micro-plasticity of the fibers may be deduced from the mechanical reaction of the material to applied static loads.
The mechanical reaction recorded for a stabilized damage state may be associated not only with a material but also with a material in a given initial damage state. This way, the micro-plastic behavior of the fibers can be recorded specifically for a given matrix damage state, implicitly taking into account stress concentrations and redistribution. Plastic energy dissipation in the fibers is expected to proceed throughout fatigue life. The amount of energy dissipated depends on the overall composite damage state, and it is proposed that the mechanical behavior of the material in a given (initial) stable damage state can be used to predict the fatigue lifetime of that damage state for given load amplitude and load ratio according to Kassapoglou's method [14]. This method makes use of plastic effects that can be estimated from the static stress-strain curve and may be used to estimate the remaining cycle lifetime before fatigue-induced fiber fractures.

8.2.2. Fatigue Testing

During the fatigue tests, internal micro-damage is progressively introduced and augmented in the specimen. The damage state progresses in the form of discrete damage events that can be monitored and characterized using AE detection. The degradation of mechanical properties can be tracked by using the

load and strain data from the testing setup and recording the cyclic hysteresis loops. Moreover, a solid AE-based damage recognition framework shall allow tracking of damage as it develops in multiple regions in the composite specimen; the AE monitoring system will, hopefully, be able to identify regions where damage is particularly dense, affecting overall stiffness of the material in that region.

As the composite degrades, it goes through a progression of damage states before final failure. Reifsnider [6] suggests that different damage mechanisms dominate the degradation of unidirectional long fiber composites at different stages of fatigue lifetime: starting with damage nucleation at locations of manufacturing defects, followed by progressive matrix cracking and fiber-matrix debonding, and finishing with final failure due to compounding fiber breakage. This narrative may be supported or rejected by the proposed fatigue tests.

9

Additional Figures

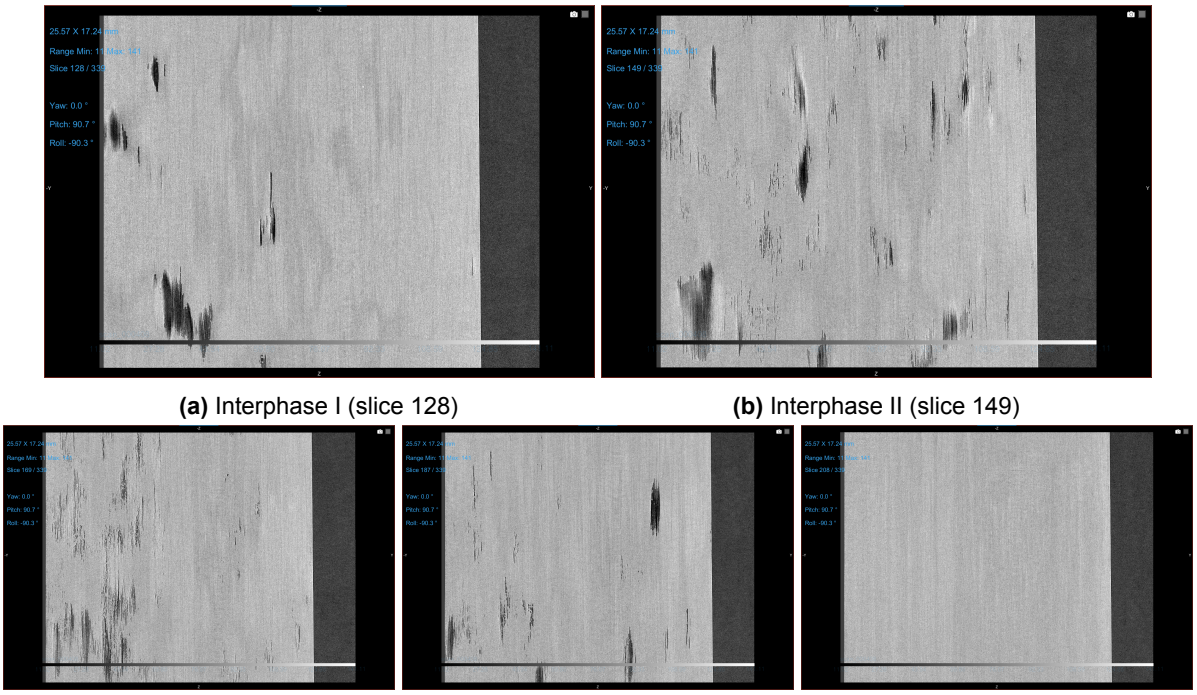

(a) Interphase I (slice 128) **(b)** Interphase II (slice 149)

(c) Interphase III (slice 169) **(d)** Interphase IV (slice 187) **(e)** Interphase V (slice 208)

Figure 9.1: Preliminary micro-CT of specimen U7 at $x = 125$ mm. Five frames showing the five ply interfaces.

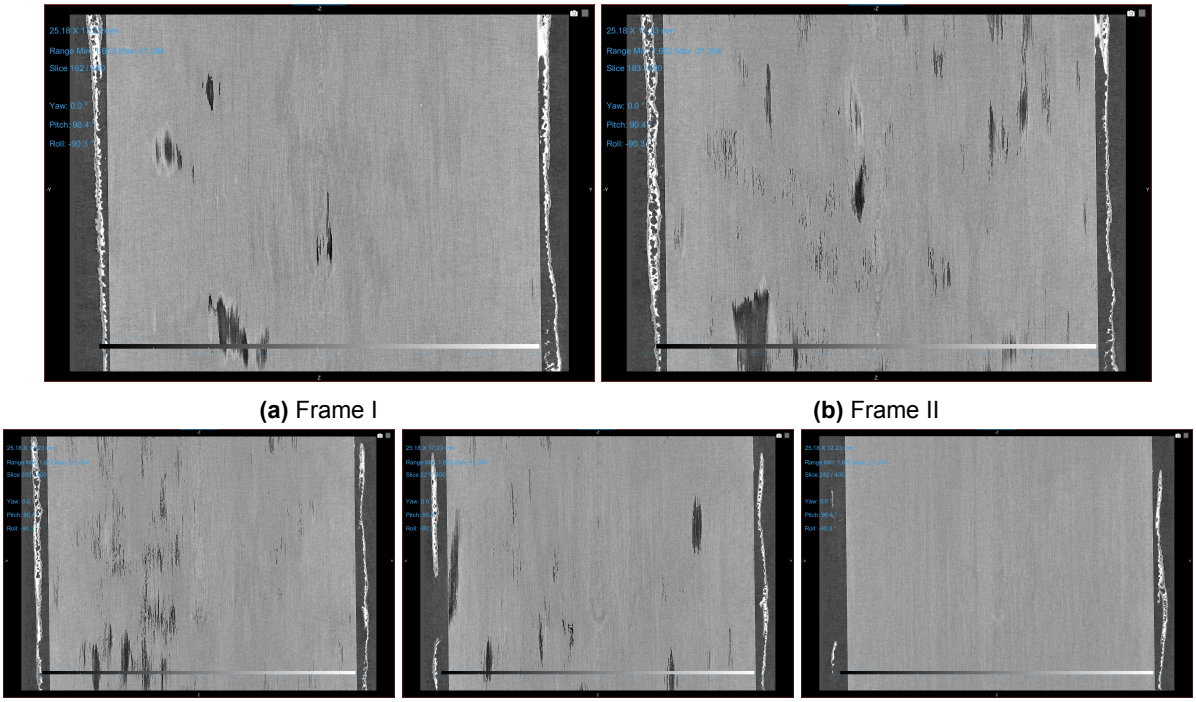

(a) Frame I **(b)** Frame II

(c) Frame III **(d)** Frame IV **(e)** Frame V

Figure 9.2: Five frames showing the five ply interfaces at the mid-length of the specimen ($x = 125$ mm) of specimen U7 after the tensile experiment.

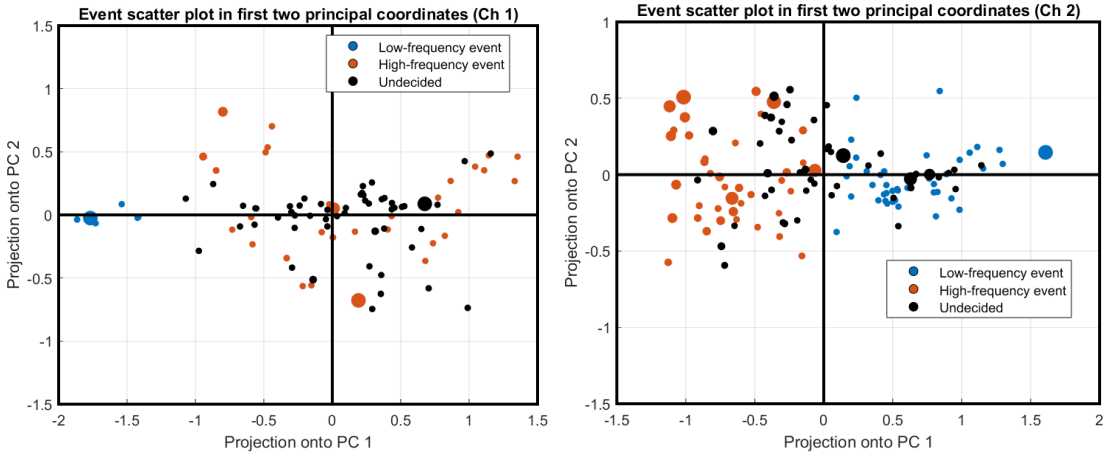

(a) Specimen U7, Channel 1. **(b)** Specimen U9, Channel 2.

Figure 9.3: Remaining two (out of the four) collected datasets projected into the 2D space of principal coordinates.

Bibliography

[1] Srinivas Sriramula et al. “Quantification of uncertainty modelling in stochastic analysis of FRP composites”. In: *Composites Part A: Applied Science and Manufacturing* 40.11 (2009), pp. 1673–1684.

[2] Simon Charles Lie. “Damage resistance and damage tolerance of thin composite facesheet honeycomb panels”. PhD thesis. Massachusetts Institute of Technology, 1989.

[3] JH Den Besten. “Fatigue resistance of welded joints in aluminium high-speed craft: a total stress concept”. In: (2015).

[4] Ramesh Talreja et al. *Damage and failure of composite materials*. Cambridge University Press, 2012.

[5] Anastasios P Vassilopoulos. “The history of fiber-reinforced polymer composite laminate fatigue”. In: *International Journal of Fatigue* 134 (2020), p. 105512.

[6] Alton L Highsmith et al. “Stiffness-reduction mechanisms in composite laminates”. In: *Damage in composite materials: basic mechanisms, accumulation, tolerance, and characterization*. ASTM International, 1982.

[7] Ramesh Talreja. “Damage development in composites: mechanisms and modelling”. In: *The Journal of strain analysis for engineering design* 24.4 (1989), pp. 215–222.

[8] CKH Dharan. “Fatigue failure mechanisms in a unidirectionally reinforced composite material”. In: *Fatigue of composite materials*. ASTM International, 1975.

[9] EK Gamstedt et al. “Fatigue damage mechanisms in unidirectional carbon-fibre-reinforced plastics”. In: *Journal of materials science* 34 (1999), pp. 2535–2546.

[10] George P Sendeckyj. “Life prediction for resin-matrix composite materials”. In: *Composite materials series*. Vol. 4. Elsevier, 1991, pp. 431–483.

[11] Joris Degrieck and et al. “Fatigue damage modeling of fibre-reinforced composite materials”. In: *Appl. Mech. Rev.* 54.4 (2001), pp. 279–300.

[12] Wim Van Paepegem et al. “A new coupled approach of residual stiffness and strength for fatigue of fibre-reinforced composites”. In: *International Journal of Fatigue* 24.7 (2002), pp. 747–762.

[13] Satrio Wicaksono et al. “A review of advances in fatigue and life prediction of fiber-reinforced composites”. In: *Proceedings of the Institution of Mechanical Engineers, Part L: Journal of Materials: Design and Applications* 227.3 (2013), pp. 179–195.

[14] Christos Kassapoglou. “Determination of energy dissipation during cyclic loading and its use to predict fatigue life of metal alloys”. In: *Fatigue & Fracture of Engineering Materials & Structures* 46.10 (2023), pp. 3667–3679.

[15] V Arumugam et al. “A global method for the identification of failure modes in fiberglass using acoustic emission”. In: *Journal of Testing and Evaluation* 39.5 (2011), pp. 954–966.

[16] Samira Gholizadeh et al. “A review of the application of acoustic emission technique in engineering”. In: *Structural Engineering and Mechanics* 54.6 (2015), pp. 1075–1095.

[17] MJ Suriani et al. “Delamination and manufacturing defects in natural fiber-reinforced hybrid composite: A review”. In: *Polymers* 13.8 (2021), p. 1323.

[18] Joseph N Zalameda et al. “Passive thermography measurement of damage depth during composites load testing”. In: *Frontiers in Mechanical Engineering* 7 (2021), p. 651149.

[19] Samira Gholizadeh. “A review of non-destructive testing methods of composite materials”. In: *Procedia structural integrity* 1 (2016), pp. 50–57.

[20] Stéphane Huguet. “Application de classificateurs aux données d’émission acoustique: identification de la signature acoustique des mécanismes d’endommagement dans les composites à matrice polymère”. PhD thesis. Lyon, INSA, 2002.

[21] Manuel Kempf et al. “Acoustic emission analysis for characterisation of damage mechanisms in fibre reinforced thermosetting polyurethane and epoxy”. In: *Composites Part B: Engineering* 56 (2014), pp. 477–483.

[22] C Muir et al. “Damage mechanism identification in composites via machine learning and acoustic emission”. In: *npj Computational Materials* 7.1 (2021), p. 95.

[23] W Harizi et al. “Damage mechanisms assessment of Glass Fiber-Reinforced Polymer (GFRP) composites using multivariable analysis methods applied to acoustic emission data”. In: *Composite Structures* 289 (2022), p. 115470.

[24] Arnaud Huijer et al. “Acoustic emission monitoring of carbon fibre reinforced composites with embedded sensors for in-situ damage identification”. In: *Sensors* 21.20 (2021), p. 6926.

[25] Arnaud Huijer et al. “Feasibility evaluation for development of composite propellers with embedded piezoelectric sensors”. In: *Marine Structures* 84 (2022), p. 103231.

[26] E Kirkby et al. “Impact localisation with FBG for a self-healing carbon fibre composite structure”. In: *Composite Structures* 94.1 (2011), pp. 8–14.

[27] Johann Kastner et al. “X-ray computed tomography for non-destructive testing and materials characterization”. In: *Integrated imaging and vision techniques for industrial inspection: advances and applications* (2015), pp. 227–250.

[28] D Baccar et al. “Identification and classification of failure modes in laminated composites by using a multivariate statistical analysis of wavelet coefficients”. In: *Mechanical Systems and Signal Processing* 96 (2017), pp. 77–87.

[29] Oleg Alexandrov. *Morlet Wavelet Mathematica*. `https://commons.wikimedia.org/wiki/File:MorletWaveletMathematica.svg`. Accessed: 2025-06-09. 2006.

[30] CR Ramirez-Jimenez et al. “Identification of failure modes in glass/polypropylene composites by means of the primary frequency content of the acoustic emission event”. In: *Composites Science and Technology* 64.12 (2004), pp. 1819–1827.

[31] Shuai Qiao et al. “Damage mode identification in carbon/epoxy composite via machine learning and acoustic emission”. In: *Polymer Composites* 44.4 (2023), pp. 2427–2440.

[32] Avik Kumar Das et al. “Machine learning based crack mode classification from unlabeled acoustic emission waveform features”. In: *Cement and Concrete Research* 121 (2019), pp. 42–57.

[33] Jie Wang et al. “A waveform-based clustering and machine learning method for damage mode identification in CFRP laminates”. In: *Composite Structures* 312 (2023), p. 116875.

[34] Richard Arnold Johnson et al. *Applied multivariate statistical analysis*. Prentice hall Upper Saddle River, NJ, 2002.

[35] Gene H Golub et al. “A generalization of the Eckart-Young-Mirsky matrix approximation theorem”. In: *Linear Algebra and its applications* 88 (1987), pp. 317–327.

[36] Anil K Jain. “Data clustering: 50 years beyond K-means”. In: *Pattern recognition letters* 31.8 (2010), pp. 651–666.

[37] Giuseppe Ciaburro et al. “Machine-learning-based methods for acoustic emission testing: A review”. In: *Applied Sciences* 12.20 (2022), p. 10476.

[38] Toray Advanced Composites. *Toray 2510 Epoxy Prepreg System Technical Data Sheet*. `https://www.toraycma.com/wp-content/uploads/2510-Prepreg-System.pdf`. Accessed: 2025-04-01. 2021.

[39] ASTM International. *ASTM D3039 / D3039M-17: Standard Test Method for Tensile Properties of Polymer Matrix Composite Materials*. https://www.astm.org/d3039_d3039m-17.html. West Conshohocken, PA, USA. 2017.

[40] International Organization for Standardization. *ISO 527-5:2009 - Plastics — Determination of tensile properties — Part 5: Test conditions for unidirectional fibre-reinforced plastic composites*. https://www.iso.org/standard/52991.html. Geneva, Switzerland. 2009.

[41] Babak Fazlali et al. “Specimen designs for accurate tensile testing of unidirectional composite laminates”. In: *Composites Part A: Applied Science and Manufacturing* 175 (2023), p. 107799.

[42] Vallen-Systeme GmbH. *Help on Vallen AE-Suite*. Software package for acoustic emission analysis. 2024. URL: https://www.vallen.de/.

[43] John Summerscales. “Acoustic emission source location in fibre-reinforced composite materials”. In: (2013).